UNIVERSITY OF OKLAHOMA

GRADUATE COLLEGE

IMPROVING DROP SIZE DISTRIBUTION RETRIEVAL AND RAIN ESTIMATION FROM
POLARIMETRIC RADAR DATA USING THE DEEP NEURAL NETWORK

A THESIS

SUBMITTED TO THE GRADUATE FACULTY

in partial fulfillment of the requirements for the

Degree of

MASTER OF SCIENCE IN METEOROLOGY

By

JUNHO HO
Norman, Oklahoma
2022

IMPROVING DROP SIZE DISTRIBUTION RETRIEVAL AND RAIN ESTIMATION FROM

POLARIMETRIC RADAR DATA USING THE DEEP NEURAL NETWORK

A THESIS APPROVED FOR THE

SCHOOL OF METEOROLOGY

BY THE COMMITTEE CONSISTING OF

Dr. Guifu Zhang, Chair

Dr. David B. Parsons

Dr. Feng Xu

Acknowledgement

List of Tables

List of Figures

Abstract

Drop size distribution (DSD) and rain rate (R) have been estimated from polarimetric radar data that are now available nationwide. DSD and R are essential in understanding rain microphysics. Past studies utilized parametrized equations or empirical formulas to estimate the parameters for DSD retrieval and R estimation. In addition, previous machine learning approaches have been utilized, but these efforts have been centered solely on rain estimation rather than estimating DSD parameters. This study focuses on estimating both DSD parameters and R using deep learning to better understand the precipitation microphysics along with an improved estimation of rain rate, which is the biggest concern in operational and societal purposes.

Past studies have found that the estimation accuracy degrades depending on errors in the radar measurements and estimation methods. Here, the deep neural network (DNN) approach has been utilized to improve the estimation of DSD and rain rate by mitigating these error effects. The performance of this approach was verified with the ground truth observations measured by a two-dimensional video disdrometer (2DVD) deployed at Kessler Farm, Oklahoma and compared with the conventional estimation methods for the period 2006−2017. Physical parameters (mass-/volume-weighted diameter and liquid water content), rain rate, and polarimetric radar variables (including radar reflectivity and differential reflectivity) were obtained from the DSD data. The three methods–physics-based inversion, empirical formula, and DNN were applied to two different temporal domains (instantaneous and rain-event-average) with three diverse error sources (fitting, measurement, and model errors). The DSD and rain estimations from the total 18 ($= 3 \times 2 \times 3$) cases were evaluated by calculating the bias and root mean squared errors (RMSE). DNN produced the best performance for most cases, up to 50% reduced RMSE when model errors existed. DSD and rain estimated from the Oklahoma City polarimetric radar using the empirical and DNN

methods were well fit to the disdrometer observations; the rain estimation bias of DNN reduced significantly (2.7% in DNN versus 6.7% in empirical). The present results suggest that DNN would be useful for retrievals from radar observation.

Table of Contents

1. Introduction

Radar data is useful in monitoring current weather situations and producing short-range forecasts by linking rain microphysics variables in the atmosphere to precipitation type and intensity (Zhang 2016). Radars are used for numerous purposes in meteorology, including hydrometeor classification (e.g., Vivekanandan et al. 1999; Liu and Chandrasekar 2000; Park et al. 2009), quantitative precipitation estimations (QPE), and drop size distribution (DSD) retrievals (e.g., May et al., 1999; Testud et al. 2000; Matrosov et al. 2005; Cao et al. 2010; Thurai et al. 2021; Ryu et al., 2021). The accurate quantification of precipitation and drop size distribution are critical for estimating latent heating (e.g., Nelson et al. 2016; Huaman and Schumacher 2018; Nelson and L'Ecuyer 2018), and further understanding and parametrization of cloud microphysics, leading to improvements of weather forecasts (e.g., Lim and Hong, 2010; Morrison and Milbrandt, 2015; Zhang et al., 2021). In the early era of radar development, only radar reflectivity (Z_h) provided the information on rain rate (R) with the well-known Z-R relationship derived using power law forms between Z_h and R. The coefficients of Z-R relation were determined depending on various factors including rain types, seasons, and locations resulting in over two hundreds Z-R relationships (Doviak and Zrnic 1993; Rosenfeld and Ulbrich, 2003). In addition, the selection of the dataset, measurement errors, and the changes in the rain microphysics led to variations in the DSDs. Typically, more parameters (≥ 2) are required to accurately characterize the DSD, leading to the development of polarimetric radars (Seliga and Bringi 1976).

The development to polarimetric radar data (PRD) provided advantageous properties that can lead to comprehensive knowledge regarding the shape, composition, and phase of hydrometeors (Zhang et al., 2019). Particular variables such as differential reflectivity (Z_{dr}) and specific differential phase (K_{DP}), and Z_h enhance the reliability of R estimation, reducing error from $30-40\%$

to ~15% (Brandes et al., 2002). Further, PRD enabled DSD retrievals by incorporating two or more radar variables. DSD can be widely used to retrieve all parameters and variables of rain microphysics and are often more useful than just R (Zhang, 2016). The deterministic retrievals using DSD parameters of slope (L) and intercept terms (N_0), from the definition of Z_{DR} (defined as $10\log_{10}(Z_{dr})$ the log unit of Z_{dr}) and Z_h are often conducted assuming two-parameter exponential or constrained-gamma DSD model (Zhang et al. 2001). However, DSD parameters are non-physical variables and not Gaussian distributed with skewed distributions (Cao et al. 2010; Zhang 2016). Mahale et al. (2019) indicated that physical parameters of mass-/volume-weighted diameter (D_m) and liquid water content (W) would be used for DSD retrieval for two-parameter exponential DSD model. These two parameters (D_m and W) can be derived from model physical parameters (number concentration and mixing ratio) which often follow a Gaussian distribution. These physics-based inversion retrievals were conducted by utilizing the parametrized PRD operators derived as function of the physical parameters (Mahale et al. 2019).

The use of PRD, empirical formula and physics-based inversion retrievals contain inherent limitations. Power law forms (i.e., empirical formula) tend to be linear in logarithmic domain, cannot handle nonlinear terms, and minimally account for measurement and/or model errors. While physics-based retrievals may perform well in the idealized formulations, these approaches do not work suitably in real atmospheric cases when errors exist. In addition, since physics-based inversion could not account for any bias in the data, small errors may significantly deteriorate its performance. This study was conducted to overcome the weaknesses of these two existing methods by introducing the deep neural network (DNN).

Here, one of the machine learning (ML) methods, DNN was applied to obtain R and physical parameters from PRD. Notice that ML has an advantage as the approach includes nonlinear terms

and additional input and output variables; so, this technique can solve complex forms of data and problems (e.g., Sarker 2021; Ho et al. 2021; Lang et al. 2021; Alimissis et al. 2018). The results can be attained from this approach quickly once the training is completed and allowing the technique to be easily employed for operational purposes. Previous studies have utilized different forms of ML for QPE. For example, Kusiak et al. (2013) demonstrated that the neural network produced the best performance among various MLs in rain estimation from Z_h alone. Shin et al. (2021) utilized random forest, a traditional ML method, to compare and improve QPE from applying the power law equations to the radar and video disdrometer data collected in Korea. Chen et al. (2020) used multilayer perceptron to estimate rain rate over a vast area from satellite-observed multi-channel radiances. However, their approach had a crucial constraint in that the technique assumed radar-retrieved R was the ground-truth. The research in this thesis used similar DNN algorithm to that of Chen et al.'s but with the inclusion of small-scale errors contained in radar variables and, several types of observational errors (i.e., measurement error and model bias) in the training and testing data sets for estimating physical parameters and R. The DNN results from this approach were compared with existing methods such as physics-based inversion retrieval and power law form of empirical formula.

The goal for this thesis can be summarized into the following three points.

- Confirm the validity of using DL algorithms for DSD retrievals and QPE

- Analyze the impact of observational errors (i.e., measurement and model errors) on the physics-based inversion, empirical, and DNN methods

- Identify if improvements result in QPE and DSD retrieval by including additional spatiotemporal or meteorological information in deep learning algorithms

In chapter 2, brief background of the variables, distributions and the parametrized PRD operators will be discussed. Chapter 3 provides a description of the data used in this investigation. Chapter 4 discusses the three methods used and compared in this research. Chapter 5 and 6 contain the results using two-dimensional video disdrometer (2DVD) and radar observations. Lastly, chapter 7 gives the summary and future works.
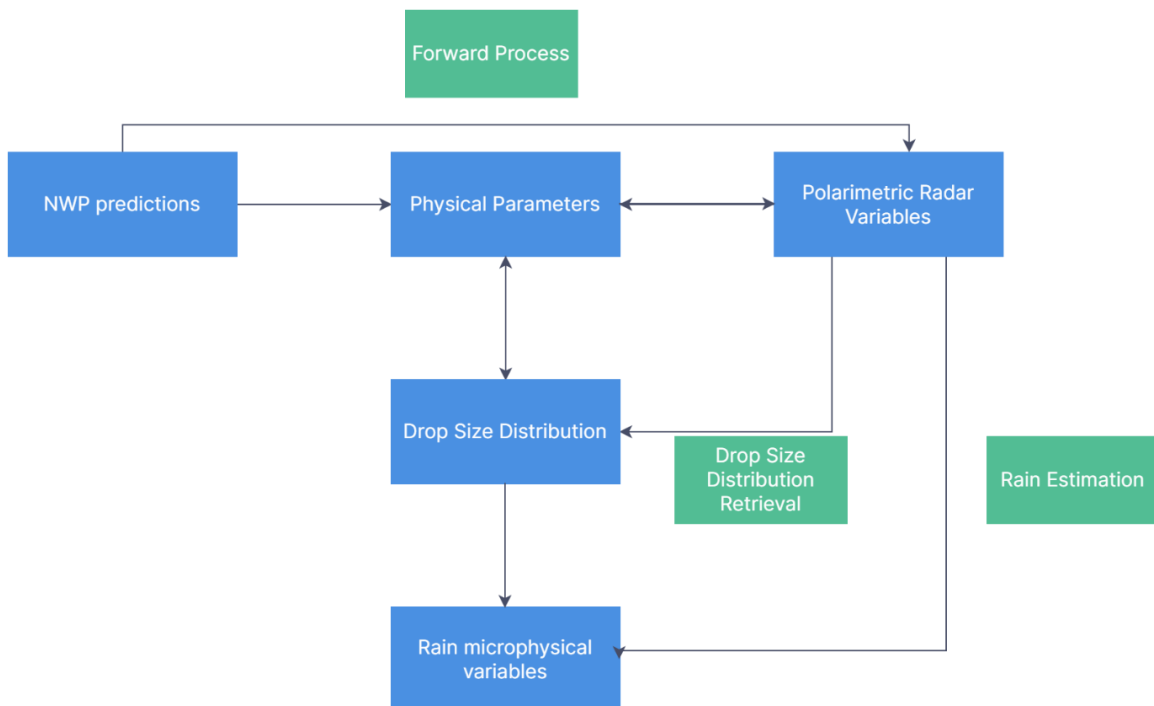
Fig 1. Flowchart displaying the forward process from NWP predictions to polarimetric radar variables, and DSD retrieval and rain estimation from polarimetric variables.

2. Background

2.1 Dual-polarimetric variables

2.1.1. Reflectivity factor

The reflectivity factor (Z) is represented by the drop size distribution (DSD) of precipitation, and can be mathematically written as

$$Z = \int_0^{D_{max}} D^6 N(D)dD \qquad (1)$$

where the D is the diameter of the droplet, N(D) the DSD, and D_{max} the maximum diameter (Kessler, 1969). The reflectivity factor is proportional to the sixth power of the diameter and can be expressed as the sixth moment. This relationship is for small spherical droplets and is derived to describe the proportional relations between radar cross section and square of the particle volume (e.g., Marzano et al., 2006). The nth moment of the DSD is represented as

$$M_n = \int_0^{D_{max}} D^n N(D)dD \qquad (2)$$

The reflectivity factor is proportional to the radar reflectivity for spherical rain particles that are small compared to the radar wavelength (i.e., Rayleigh scattering). The radar reflectivity factor is expanded further to include the radar polarimetry, random orientation, and the DSD (Danielsen et al. 1972; Smith et al. 1975; Doviak and Zrnić 1984; Zhang 2016). Then, assuming S-band and raindrop shape from Brandes et al. (2002), the effective reflectivity factor for horizontal and vertical polarization are expressed by

$$Z_{h,v} = \frac{4\lambda^4}{\pi^4 |K_w|^2} \int_0^\infty \left| s_{hh,vv}(\pi, D) \right|^2 N(D)dD \qquad (3)$$

$$\text{for } K_w = \frac{\varepsilon_r - 1}{\varepsilon_r + 2} \qquad (4)$$

and in decibels (dBZ),

$$Z_{H,V} = 10 \log_{10} Z_{h,v} \qquad (5)$$

where the λ is the wavelength (mm), N(D) the DSD (m^{-3}mm^{-1}), K_w (Eq. 4) the complex dielectric constant for water, and the s_{hh} and s_{vv} the backward scattering amplitudes for horizontal and vertical polarization, respectively (Doviak and Zrnić 1984). The Z_h (Eq. 3) is in linear units of mm^{6}m^{-3} and the Z_H (Eq. 5) in the logarithmic units of dBZ. Note that Eq. 3 can be simplified to the form of Eq.1 for small particles (D $< \lambda/16$) in Rayleigh scattering regime of spherical particles. Z_H contains the concentration of rain, and the intensity of rain can be obtained. Z_H is the quantity of the returning radar energy back to the radar from the target, and depends on various factors such as number, size, shape, dielectric property, and symmetry of the hydrometeors. Due to this variability, Z-R relationship depended on too many factors requiring additional polarimetric variable for accurate QPE.

2.1.2. Differential Reflectivity

The differential reflectivity (Z_{DR}) indicates the ratio (Z_{dr}) between the horizontal (Z_h) and vertical radar reflectivity (Z_v) in decibel, which can be written as

$$Z_{DR} = 10 \log_{10}(\frac{Z_h}{Z_v}) \qquad (6)$$

where the Z_h and Z_v are the horizontal and vertical components displayed in Eq. 3 (Seliga and Bringi, 1976). Similar to Z_H, the Z_{DR} is Z_{dr} in dB unit. Z_{DR} contains information regarding the shape and size of the rain droplets, further providing information regarding the rain microphysics. From equation 6, it is intuitive to notice that Z_{DR} is positive for larger scatter from the horizontal, negative for larger scatter from vertical, and zero if spherical shaped. Starting from Seliga and Bringi (1976), Z_{DR} is widely used for QPE purposes and DSD retrievals (e.g., Seliga et al. 1979; Ulbrich and Atlas 1984; Zhang et al. 2001, Cao et al. 2008). In rain, Z_{DR} also typically increases

with heavier rain and Z_H, but may display large Z_{DR} and relatively moderate Z_H in cases of size sorting in the leading convective regions (Kumjain et al. 2013). Generally, tropical rain has smaller rain drops (i.e., smaller Z_{DR}) and continental rain larger rain drops (e.g., Ryzhkov et al. 2005b; Tokay et al. 2008; Ryzhkov et al. 2011).

2.1.3. Additional polarimetric variables

The specific differential phase shift (K_{DP}) is defined as the phase difference between the horizontal and vertical components across a unit distance and is expressed as

$$K_{DP} = \frac{180\lambda}{\pi} \times 10^{-3} \int Re[s_{hh}(0,D) - s_{vv}(0,D)]N(D)dD \qquad (7)$$

where $s_{hh,vv}$ (mm) are the forward scattering amplitudes each for horizontal and vertical polarization, and the parts within Re the real part of the differences in scattering amplitudes. K_{DP} is often used for QPE purposes due to its usefulness in heavy rain and less sensitivity to hail contaminations (Sachidananda and Zrnić 1987; Ryzhkov and Zrnić 1996). However, K_{DP} does not work well for light rain, often contains large error, and the resolution volume is different compared to Z_H and Z_{DR} (Ryzhkov et al. 2005a). The co-polar radar correlation coefficient represents the similarity between the horizontal and vertical components of polarization and is expressed as

$$\rho_{hv} = \frac{\int s_{hh}^*(\pi,D)s_{vv}(\pi,D)N(D)dD}{\left[\int |s_{hh}(\pi,D)|^2 N(D)dD \int |s_{vv}(\pi,D)|^2 N(D)dD\right]^{1/2}} \qquad (8)$$

While ρ_{hv} are useful in qualitatively classifying hydrometeors, ρ_{hv} is close to 1 for rain at S-band frequencies and is not useful for quantitative processes of QPE or DSD retrieval. Thus, most of the calculations and estimations hereafter are predominantly conducted as functions of Z_h and Z_{dr}, which have the highest data quality.

2.2. Drop size distribution

The DSD describes the fundamental of rain microphysics and can be used to calculate rain physics parameters (Zhang 2016). The Marshall-Palmer (M-P), exponential, and gamma DSD distribution models had been widely used to describe rain microphysics utilizing the number concentration parameter (N_0, $mm^{-\mu-1}$ m^{-3}), slope parameter (L, mm^{-1}), and for gamma distribution, shape parameter (μ). The one parameter, M-P model has one unknown parameter L with fixed N_0 of 8000 m^{-3} mm^{-1} (Marshall and Palmer 1948; Kessler 1969) and is written as

$$N(D) = 8000exp\,(-\Lambda D) \qquad (9)$$

The three-parameter gamma DSD distribution is also used to describe rain DSD (Ulbrich 1983). Gamma DSD model is useful in representing broader range of rain DSD. Noting that all three parameters are not independent of each other (Haddad et al., 1996), the constrained-gamma (C-G) DSD distribution model is proposed in order to facilitate the process of retrieving three parameters from radar measurements (Zhang et al. 2001). The gamma DSD and the relation between shape and slope parameters for Oklahoma (Cao et al. 2008) are derived as following

$$N(D) = N_0 D^\mu exp\,(-\Lambda D) \qquad (10)$$

$$\mu = -0.0201\Lambda^2 + 0.902\Lambda - 1.718 \qquad (11)$$

While the three parameter C-G DSD distribution model is better in displaying natural rain, the two parameter, exponential model is still predominantly used in numerical weather prediction (NWP). The exponential DSD distribution is mathematically written as

$$N(D) = N_0 exp(-\Lambda D) \qquad (12)$$

The N_0 and L terms are commonly referred to as the DSD parameters. The DSD retrieval is conducted by calculating the DSD parameters from radar variables to form the DSD based on the DSD distribution models. DSD parameters are nonphysical parameters and often have skewed distributions. Mahale et al. (2019) suggested the usage of mass-/volume- weighted mean diameter (D_m) and liquid water content (W), also called the physical parameters, for the two-parameter exponential DSD model. The advantage of using physical parameters is that they can be obtained from rainwater mixing ratio and number concentration from NWP simulations and are often gaussian distributed (Mahale et al. 2019).

3. Data

The quality, and inclusion of errors and contamination is a core part in training the DNN and forming the equations for the empirical formulas. Here, the 2DVD, and operational S-band radar observation data are utilized. The initial training is conducted using the 2DVD data, which often contains less errors and contamination, and the observational errors can be controlled to observe the effects on the different methods. Then, the three methods will be tested on the operational radar data.

3.1. Disdrometer data

The rain microphysics variables from two-dimensional video disdrometer (2DVD) for the period 2006–2017 (twelve years) were analyzed for initial model evaluations. 2DVD can directly measure microphysics variables such as DSD, and particle size in approximately one-minute

interval. The 2DVD works by projecting two orthogonal light sheets onto two cameras and when particles fall through the two light sheets and recording the shadows on to the photodetectors (Kruger et al. 2001). The sampling volume of the 2DVD can be calculated by multiplying the sampling cross section, fall velocity, and sampling interval (Campos and Zawadzki, 2000). The cross section is 0.01 m^2 and the sampling volume of the 2DVD is typically less than 5 m^3 for each minute. Given the observed DSD data and T-matrix scattering amplitudes for S-band radar, radar variables (e.g., Z_H, Z_{DR}, K_{DP}), and rain microphysics parameters (e.g., D_m, W) were calculated from numerical integration of wave scatterings. The 2DVD used in this research is located in Kessler Farm Field Laboratory (KFFL; 34.98°N and 97.53°W), about 44.75 km southwest (239 degrees) of the KTLX Oklahoma City radar (Fig. 2). During the twelve years, the total of 616320 points were collected over 428 days of rain events.

3.2. Radar data

The polarimetric measurements from the S-band KTLX Weather Surveillance Radar-1988 Doppler (WSR-88D, also called as NEXRAD), with a beamwidth of 0.95° and a range resolution of 250 m, were used to compare the performance of each method on radar observations for the same dates as 2DVD beginning 2013. The data prior to 2013 were removed due to lack of polarimetric radar variables. The NEXRAD level-II data was obtained from National Center for Data Collection (www.ncei.noaa.gov) for only the lowest 0.5° elevation above the corresponding 2DVD location. This data included several mesoscale convective system cases of both stratiform and convective rain. The radar sampling volume were calculated by multiplying the beamwidth, gate size, and distance from the radar. The radar data were updated approximately in five-minute intervals, and the radar resolution volumes are about 10^7 larger than the sampling volume of 2DVD

at a distance of 30 km (Cao et al. 2008). In addition to difference in spatial/temporal resolution, radar data are often prone to additional sources of contamination such as hail, ground clutter, and anomalous propagation (Ulbrich and Lee 1999; Hubbert et al. 2009; Grams et al. 2019; Zhang et al. 2020).
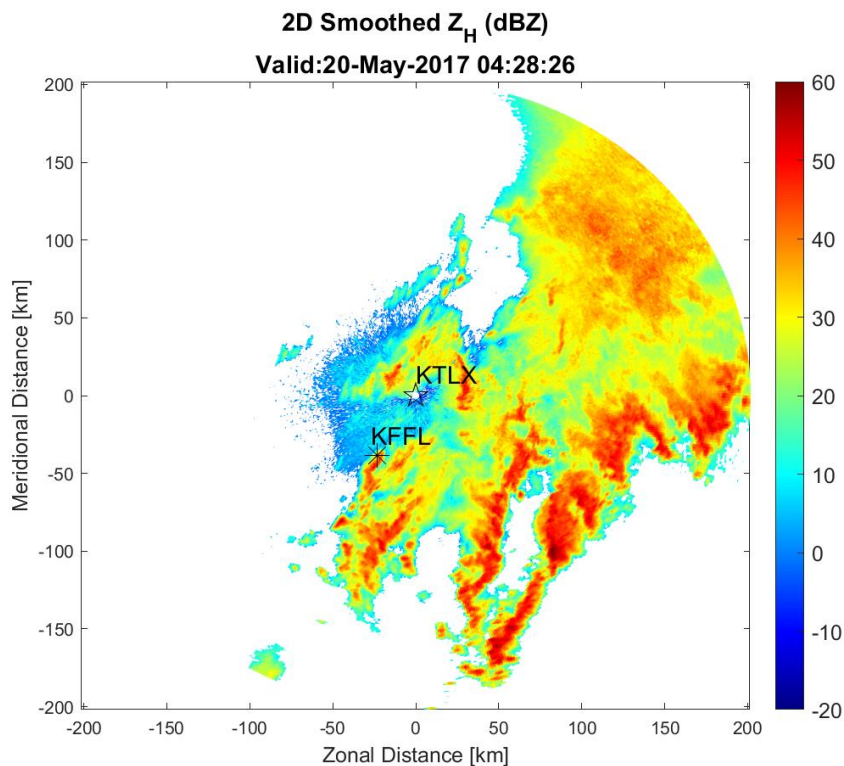
Fig 2. Plot of Z_H on May 20th, 2017 at 04UTC displaying the locations of 2DVD and KTLX radar.

3.3. Data collection

To minimize the error from the observations, unrealistic (e.g., rain rate over 1000 mm hr^{-1}) and non-meaningful (e.g., rain rate below 0.1 mm hr^{-1}) rain events were excluded. Some unrealistic values were in the 2DVD data, because 2DVD collects data every minute, and high rain rate values may be recorded in a single time frame. For 2DVD data, which typically has less error sources than radar data, rain events within the range of R between 0.1 and 100 mm hr^{-1}, the total

count larger than 50, and Z_{DR} between 0.2 and 4.5 dB were considered. When conducting the average, rain events that continued for at least twenty minutes, allowing ten minutes interruption, were grouped. The Z_{DR} range was limited, because exponential DSD model does not accurately represent both very small and large droplets from natural rain (Ulbrich 1983, Kozu and Nakamura 1991, Tokay and Short 1996). When temporal information was included for rain estimation or DSD retrieval, all rain events were divided into twenty minute sequences to ensure sufficient amount of data and match the size of input data. For all cases, data were divided into 70%, 15%, 15% for training, validation, and testing, respectively. The total of 595 rain events were selected and 54,112 points were available for training process. It is noted that number of samples for the total training was diverse for different error cases due to the exclusion of values outside the chosen criteria. During the training process when choosing appropriate weighting and form of empirical formulas and selecting the activation function and input form and unit for DNN, 2DVD data were used.

In order to compensate for the increased sources of errror and contamination, some filtering and averaging were applied on the raw radar data. First, the five-point median filter over five gates along the radial were used to remove flattation error and smooth the data. Second, radar correlation coefficient (ρ_{hv}) filter was applied to minimize the influence of hail and non-meteorological objects (e.g., ground clutter and beam blockage). Then, the averaged Z_h and Z_{dr} values over the five gates (two gates prior to and two after the estimated corresponding location), excluding missing values, were utilized as the input data. The DSD data from 2DVD (in one-minute interval) were modified to adjust the radar data (in five-minute interval) by using the corresponding time and the next four minutes. Within these five minutes DSD data, both maximum and minimum values were discarded and the mean of the remaining three has been used to retrieve the D_m, W, and R using numerical

integration. These procedures were conducted to lessen the impact of different spatiotemporal resolution between radar and 2DVD, resulting in reduced flattation error, and accomodation of the time lag from different starting angle of the radar beam and the observation height between 2DVD and radar (approximately 400 m higher at the corresponding location). The anomalous propagation or hail contamination from nearby gates may still influence the data at the chosen location. Only gates with ρ_{hv} values larger than 0.97 are considered, and filtered again before usage.

3.4. Three types of error

The perfect, measurement, and model errors were introduced to examine the influence of different errors in estimations, and the performance of the three methods. First, no external errors were introduced. The perfect error in each methods purely occurs from the fitting process between the radar variables and the three estimators. Mahale et al. 2019 derived the parametrized PRD operators for rain by assuming exponential DSD distribution, as function of D_m (in mm) and W (in 1 g m^{-3}) as

$$Z_h = W(-0.3078 + 20.87D_m + 46.04D_m^2 - 6.403D_m^3 + 0.2248D_m^4)^2 \qquad (13)$$

$$Z_{dr} = 1.019 - 0.1430D_m + 0.3165D_m^2 - 0.06498D_m^3 + 0.004163D_m^4 \qquad (14)$$

The radar variables are expressed in polynomial functions of physical parameters for the convenience of usage. The process of calculating the input and output variables for perfect error category is conducted as following. The input radar variables, Z_h and Z_{dr}, are simply calculated using Eqs. 13 and 14 for given D_m and W. Taking truncation effects of DSD into account, the output variables, physical parameters and R, are formed by utilizing D_m and W to calculate the DSD parameters (Eqs. 15 and 16), which can be further used to calculate the DSD (i.e., N(D) in Eq. 12) assuming exponential DSD distribution,

$$\Lambda = -\frac{0.00065}{D_m^2} + \frac{4.01}{D_m} - 0.023 + 0.028D_m - 0.01D_m^2 \qquad (15)$$

$$N_0 = \frac{6\times10^3 W\Lambda^4}{\pi\gamma(\lambda D_{max},4)} \qquad (16)$$

where Λ is the slope parameter, D_m mass-/volume- weighted diameter, N_0 intercept parameter, W liquid water content, and D (mm) particle diameter. The calculated DSD are then numerically integrated to form physical parameters and R. The fitted relations are matched well with the numerically calculated values in figure 1. All procedures and equations above are derived based on the definitions of physical parameters assuming exponential DSD model and accounting for truncation effects. Additional details regarding the parametrized PRD operators can be found in Mahale et al. (2019).

Second, the statistical Gaussian distributed external errors were introduced to the radar variables calculated in the previous step. The standard deviation of the errors for Z_H was 1 dBZ, and 0.2 dB for Z_{DR}. No additional errors were included to the estimators.

Third, for model error category, random errors arising from 2DVD observations were included. The included errors encompasses some measurement errors as well as the model errors arising from the difference between the modelled exponential DSD and the measured rain DSD, and the difference of radar variables between the numerical integrations and using the parameterized operators. The numerically integrated radar variables, physical parameters, and R directly calculated from 2DVD DSD observations were used for the analysis.

3.5. Evaluation metrics

The evaluation metrics include bias, root-mean-square-error (RMSE), absolute error, and bias factor. Bias is the difference between estimated and observed mean values (Eq. 17). RMSE is the

root of the average of the squared sum of the difference between observation and estimation (Eq. 18). Here, the relative bias and RMSE are expressed in percentage by dividing the mean of the observed values. The percent values may reduce excessive influence from large differences in a small sample. The residual represents the difference between estimation and observation for each points (Eq. 19). The bias factor is the ratio of summed estimation to summed observation (Eq. 20); it has been frequently used in previous studies (Brandes et al. 2002).

$$Bias = \frac{1}{L}\sum_{\ell=1}^{L}[x_{est}(\ell) - x_{obs}(\ell)] \qquad (17)$$

$$RMSE = \sqrt{\sum_{\ell=1}^{L}\frac{1}{L}[x_{est}(\ell) - x_{obs}(\ell)]^2} \qquad (18)$$

$$Residuals = x_{est} - x_{obs} \qquad (19)$$

$$Bias\ Factor = \frac{\sum_{\ell=1}^{L}[x_{est}(\ell)]}{\sum_{\ell=1}^{L}[x_{obs}(\ell)]} \qquad (20)$$

4. Methods

4.1. Physics-based Inversion

The physics-based inversion method utilizes the parameterized PRD operators (Eqs. 13 and 14) taken from Mahale et al. (2019). This method provides the most interpretability because the entire procedure is formulated based on the definitions and observed relations between the physical parameters and radar variables (Fig. 3). The entire process is constituted of two parts, calculation of physical parameters from parametrized PRD operators and retrieval of microphysics variables from the calculated physical parameters. The former process is the direct inversion of Eqs. 13 and 14, using the root of nonlinear function. For a given Z_{dr}, the best representation of D_m is calculated

from the relation in Eq. 14. Subsequently, the calculated D_m and given Z_h can be used to calculate W from Eq. 13. The calculated D_m and W can be further utilized to form the DSD parameters and DSD from Eqs. 15 and 16. Then, the DSD is used to retrieve all necessary rain microphysics variables, including R, using numerical integration. Since this approach does not utilize additional data or include error terms to adjust the relations for different sets of data, the equations derived from the physical models does not always represent the real situations. Thus, this approach lacks flexibility for various weather phenomenon. While this method is based on the two-parameter exponential DSD distribution, the performance of the physics-based inversion method is conducted for the C-G distribution (Table 1). The mu-lambda relation (Eq. 11) for Oklahoma was used based on the Cao et al. 2008. The percentage RMSE using C-G model reduced 8.9% for D_m, 23.7% W, and 5.3% R compared to that of the exponential model. This result agrees with previous research where C-G distribution is more fit to describe natural rain (Zhang et al. 2001).

Table 1. The percentage RMSE of the error estimation for the three variables (D_m, W, and R) using exponential and constrained-gamma (C-G) distributions.

	Exponential distribution			C-G distribution		
	D_m	W	R	D_m	W	R
RMSE (%)	28.2	115.4	86.8	19.8	91.7	81.5
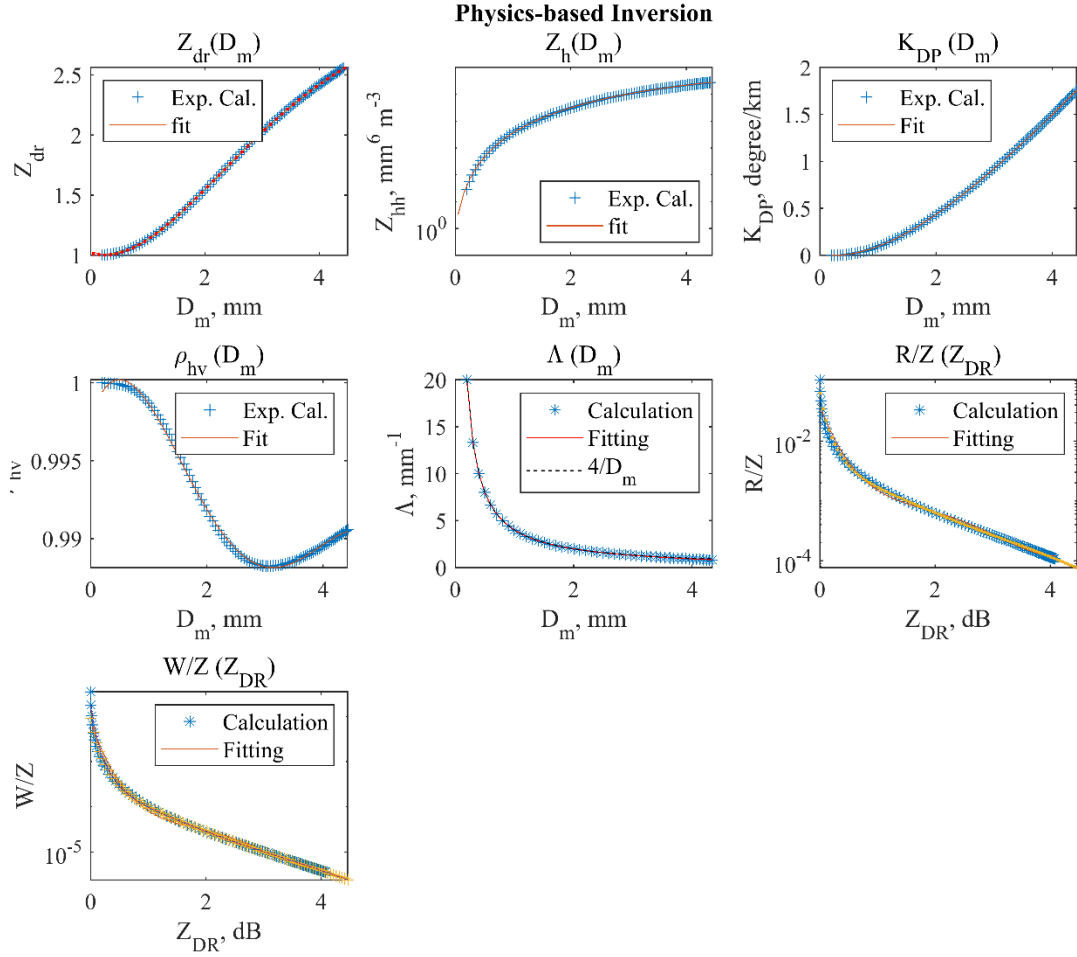
Fig. 3. Scatter plots of numerical calculations and polynomial fitting as functions of mass-/volume-weighted mean diameter (D_m) and liquid water content (W) for (a) Z_{dr}, (b) Z_h, (c) K_{DP}, (d) r_{hv}, (e) L, (f) R/Z, (g) W/Z. The unit for D_m is mm, Z_h mm^6 m^3, K_{DP} km^{-1},

4.2. Empirical method

The empirical formulas are commonly used for operational purposes due to its intuitiveness and simplicity (Grams et al. 2019; Ryzhkov et al. 2022). Both power law and polynomial forms were often adopted for rain estimation (Brandes et al. 2002; Cao et al. 2008; Ryzhkov et al.2022). In this study, proper formulations of both forms were conducted and evaluated. Starting with the

power law form, the exponent of 0,1, 1.5, and 2 of the estimating parameters were utilized as the weighting for the estimations (Table 2). The power law forms were derived using the least squares fit in known covariance method with appropriate weighting. The weighting is necessary to accommodate for less frequent large values of physical parameters and R. Based on the percentage bias and RMSE results in Table 2, the exponent between 1 and 1.5 will provide the best results.

Table 2. The training results of different weighting for the power law forms displayed in percentage bias and RMSE of the three estimators (D_m, W, and R)

	0			1			1.5			2		
	D_m	W	R	D_m	W	R	D_m	W	R	D_m	W	R
Bias (%)	-0.1	-13.2	-11.4	1.0	3.6	1.6	2.0	6.0	2.1	3.4	6.2	1.1
RMSE (%)	21.0	80.9	73.4	16.4	44.9	34.1	15.5	42.6	31.1	15.2	44.0	31.3

Different weights for power law
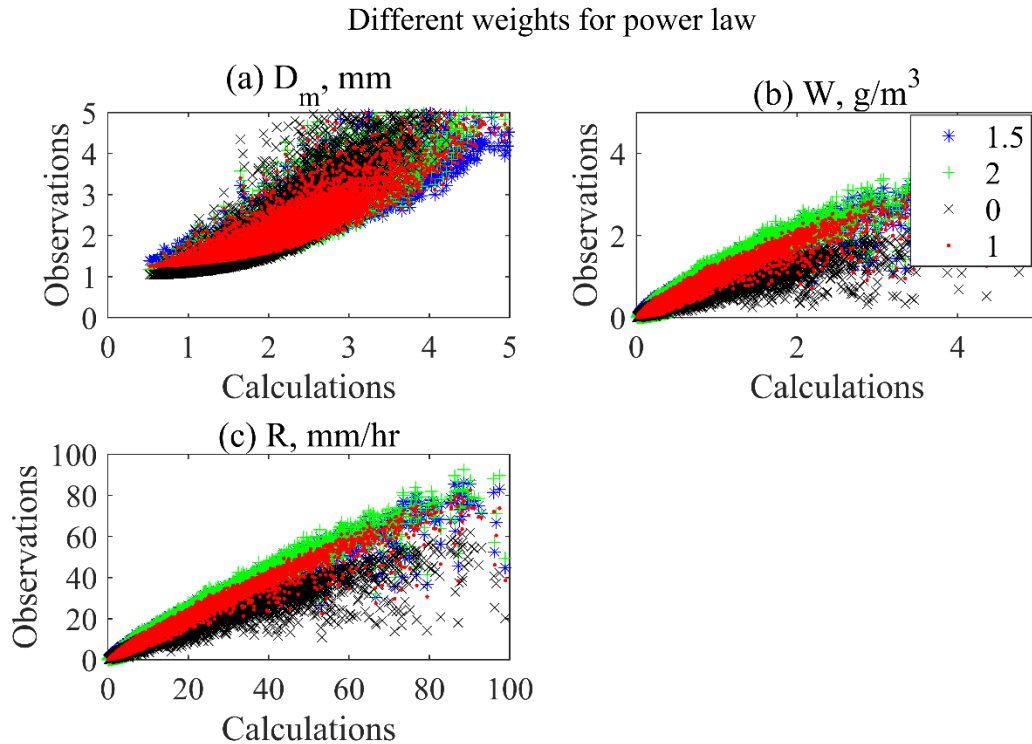
Fig. 4. Scatter plot of different weights for power law form of empirical formula for estimating (a) mass-/volume-weighted diameter (D_m), (b) liquid water content (W), and (c) rain rate (R). The unit for D_m is mm, W g m^{-3}, and R mm hr^{-1}. The blue star denotes

However, for simplicity, the exponent of 1.5 of the estimators was chosen. The exponents of 1 and 1.5 most resemble a straight line in one-one plot, with no weighting and exponent of 2 estimating too small or large for higher values (Fig. 4). Typically, the estimation results for W and R should be similar, because W is the third and R the 3.67th DSD moment. The results in table 2 display large difference between the W and R estimation as the exponents increased due to such small values of W. The R worked as a good weighting for W estimation reducing more than 5% bias and similar RMSE for exponent of 1.5 (Table 3). Thus, the weightings were chosen as R$^{1.5}$ for all three estimators using the power law form.

Table 3. The percentage bias and root mean square error (RMSE) for different weights of liquid water content (W) and rain rate (R) when estimating W using power law form of empirical formula. Each data point is weighted based on the least squares solution of known covariance.

	W			R		
	1	1.5	2	1	1.5	2
Bias (%)	3.6	6.0	6.2	1.2	0.9	-1.3
RMSE (%)	44.9	42.6	44.0	43.2	41.0	41.6

Next, the polynomial and power law forms of empirical formulas were tested on the entire 2DVD dataset. Relative errors were calculated, which are the errors divided by the mean observed values, i.e., Eqs. (17)-(18) are divided by the mean observation. The training and testing relative RMSE and bias for single polarization Z-R relationship, power law and polynomial forms using dual-polarization variables were calculated and recorded in tables 4 and 5. Although the training bias for single-polarization was as low as 0.93%, the testing bias was 6.6% exceeding 0.6% using dual-polarization variables. The power law was found to perform better than the polynomial for W and R estimations when adequate weighting was selected for the power law forms. Lower biases were observed, with 0.9%, 2.1% bias for power law compared to 3.2%, 2.3% from polynomial forms. The RMSE was about 6% lower in power law for both training and testing W and R estimations. For D_m estimation, polynomial form resulted in less error with no bias and 9.6% RMSE. The RMSE is still lower using polynomial form, similar bias is observed on testing data. The figures 5 and 6 display a scatter plot of power law and polynomial forms for the three estimations. Some differences can be found in the regions of higher values, where polynomial form tends to overestimate, and power law underestimate. Thus, only power law forms are used hereafter.

Table 4. The rain estimation results using single polarization variable, dual polarization variables in power law and polynomial forms for D_m, W, and R estimations.

	Single polarization	Dual-polarization Power law (1.5)			Dual-polarization polynomial		
	R	D_m	W	R	D_m	W	R
Bias (%)	0.93	2.0	0.9	2.1	0.0	3.2	2.3
RMSE (%)	94	15.5	41.0	31.1	9.6	46.9	37.6

Table 5. Same as Table 4 except for testing data.

	Single polarization	Dual-polarization Power law (1.5)			Dual-polarization polynomial		
	R	D_m	W	R	D_m	W	R
Bias (%)	6.64	0.3	1.1	0.6	0.1	-0.2	0.6
RMSE (%)	102.6	15.4	47.4	35.4	9.6	49.0	39.1

Power law vs. Polynomial training

(a) D_m, mm

(b) W, g/m^3

(c) R, mm/hr
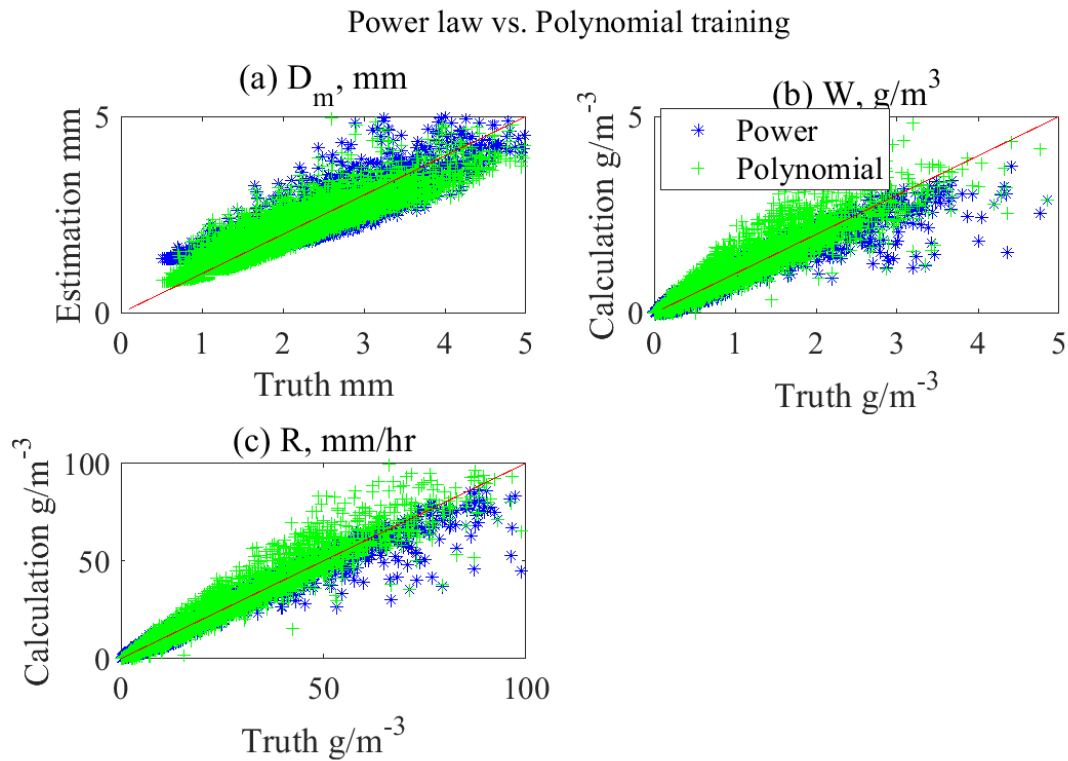
Fig. 5. Scatter plot of the estimations of three estimators, (a) D_m, (b) W, and (c) R using power law and polynomial forms of empirical formulas. The blue star denotes the power law, and the green plus sign polynomial form.

Power law vs. Polynomial
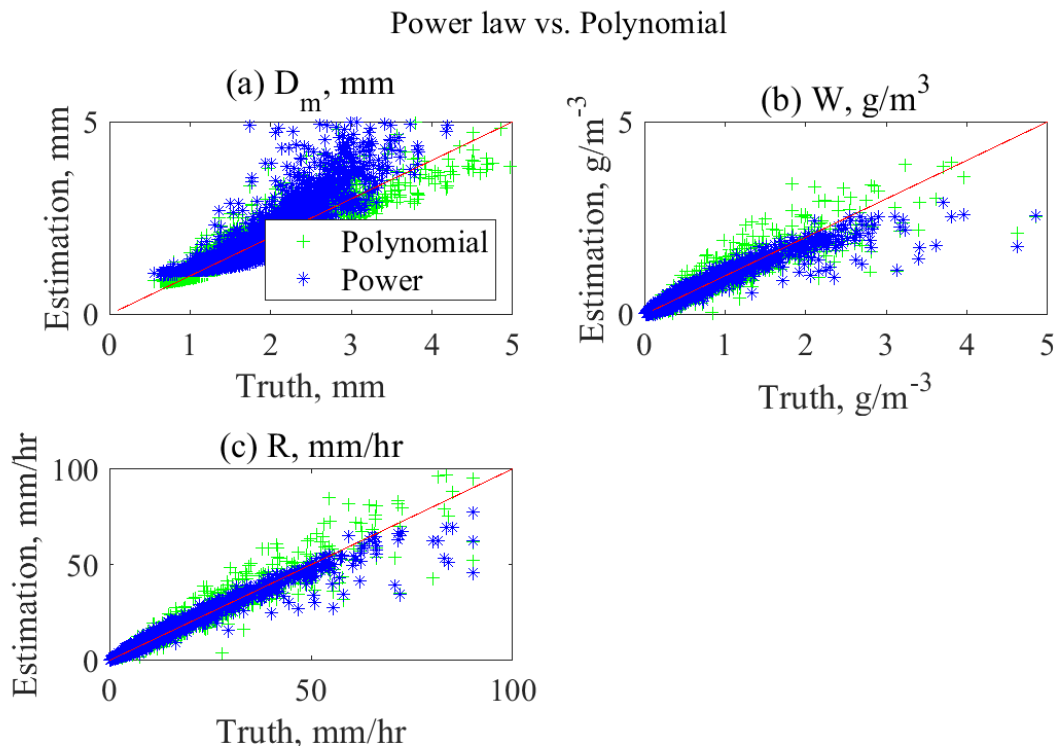
Fig. 6. Same as Fig. 5 but for testing results.

The empirical formulas of physical parameters and R for perfect, adding measurement, and with model errors were derived in Table 6. The table 6 indicates that D_m mainly relies on the positive exponent of Z_{dr} for estimation. The exponent of Z_h is small for all error types of D_m estimation, ranging from 0.011 to 0.028. This is because D_m is a size property, which is mainly contained in Z_{dr} (Kumjian, 2013). Although D_m is often derived as function of Z_{dr} only, the results show that inclusion of Z_h provide better performance (not shown). The power law forms for W and R display positive exponent for Z_h, and negative for Z_{dr} displaying inverse relations. The empirical formulas for W and R estimations display similar form of equations because W is third and R approximately 3.67^{th} DSD moment. The exponent of Z_h is larger for W and R, because those

two contains physical information of the number concentration of droplets (Kumjian, 2013). The constant term of D_m is much larger than that of W and R, from 0.81 to 1.01.

Table 6. Empirical formulas of mass-/volume-weighted diameter (D_m), liquid water content (W), and rain rate (R) for perfect, adding measurement, and with model errors. All formulas were derived using two-dimensional video disdrometer data in Kessler Farm Field Laboratory, Oklahoma for the period 2006–2017.

	D_m	W	R
Perfect error	$0.90Z_h^{0.011}Z_{dr}^{1.6}$	$0.00039Z_h^{0.95}Z_{dr}^{-4.4}$	$0.0049Z_h^{0.97}Z_{dr}^{-3.7}$
Adding measurement error	$0.80Z_h^{0.037}Z_{dr}^{1.2}$	$0.001Z_h^{0.79}Z_{dr}^{-2.9}$	$0.0096Z_h^{0.85}Z_{dr}^{-2.5}$
With model error	$0.98Z_h^{0.046}Z_{dr}^{0.91}$	$0.00059Z_h^{0.83}Z_{dr}^{-3.0}$	$0.0072Z_h^{0.89}Z_{dr}^{-3.04}$

Empirical formulas are relatively easy to formulate and provides interpretable equations between the variables. In addition, power law forms can be derived for different sets of data, providing more flexibility compared to the previous physics-based inversion method. In addition, some model, measurement errors, and prior probability density function (PDF) are included compared to the physics-based method. However, there are several limitations, for optimal results the error in the logarithm domain needs to be Gaussian distributed to be optimal. Also, the bias, errors and prior can be additionally and more effectively incorporated using statistical or ML methods. Notice that the linear relationship between the radar variables and rain rate in logarithmic domain does not show accurate results in linear domain (Zhang et al. 2019). Figures 7 and 8 display the D_m, W, and R estimation results for training and testing sets in linear and logarithmic domain. While linear line is observed in logarithmic domain, the estimated points are dispersed in linear domain, especially for the single polarization case, resulting in more errors in linear domain.
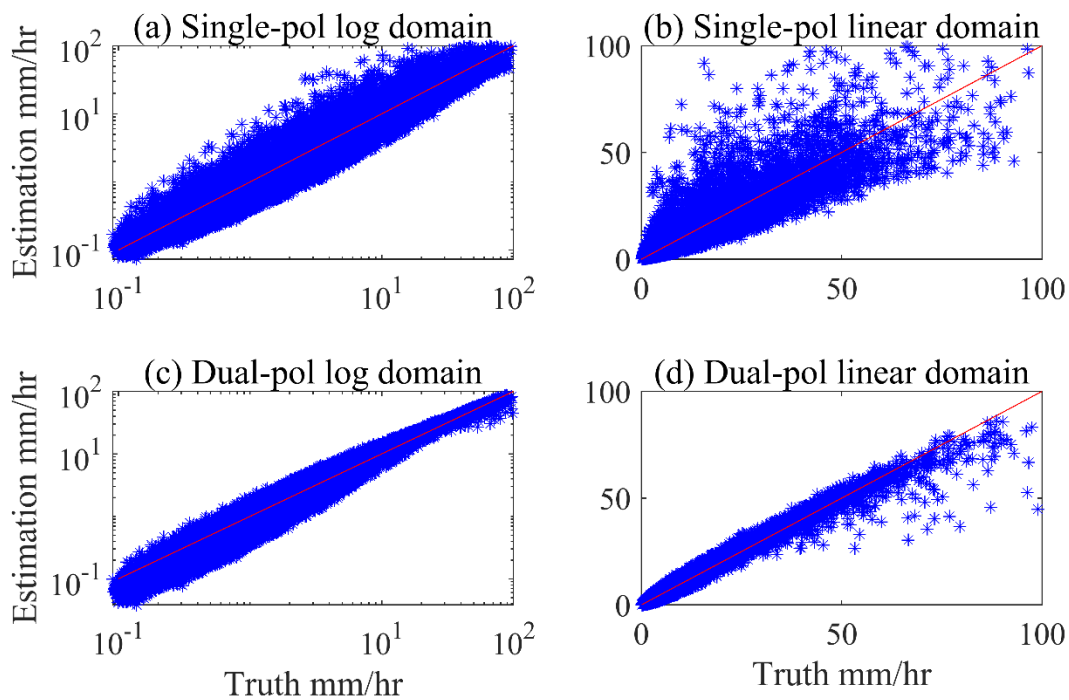
Fig. 7. Scatter plots of rain estimation using single polarization (only radar reflectivity; a and b) and dual polarization (both radar reflectivity and differential reflectivity, c and d) radar variables in logarithmic (a and c) and linear domain (b and d). The results were calculated based on the training dataset. The units are mm hr^{-1}.

Log vs. Linear domain (testing)
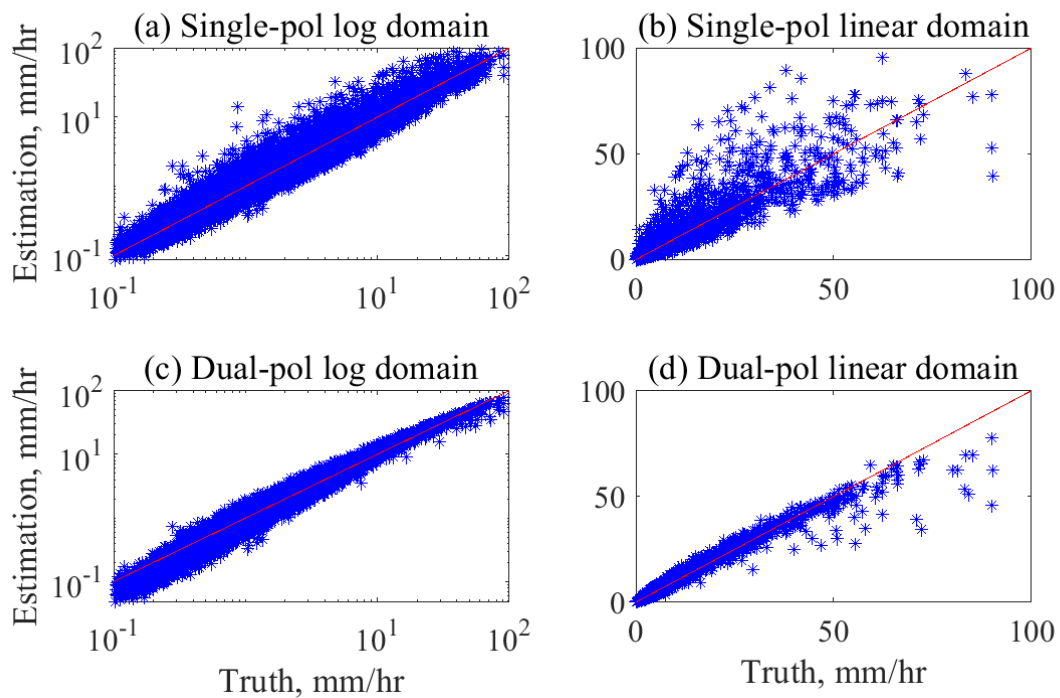
Fig. 8. Same as Fig. 7 but for testing data.

4.3. Deep Neural network
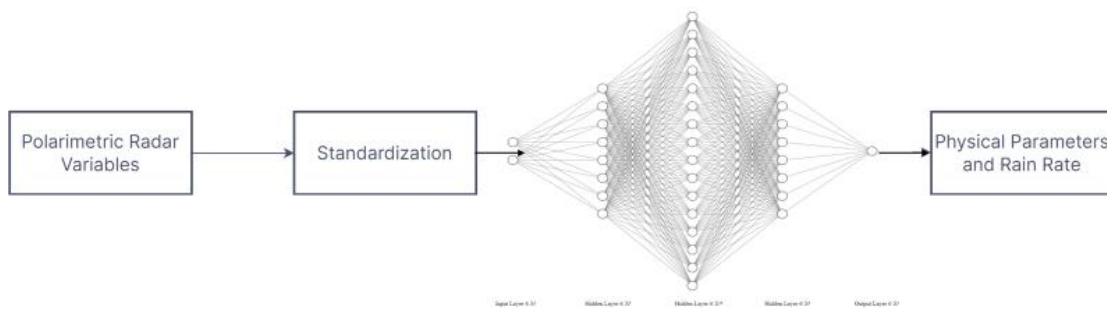
Fig. 9. Architecture of the deep neural network for estimating physical parameters and rain rate from polarimetric radar variables. The box displays the hyperparameters used in the model. The 16 different architectures, with batch size of 64, learning rate 0.01, and fixed number of epochs of 120, and hyperbolic tangent function (Tanh) is used as the activation function in the hidden layers.

Various forms and types of ML and deep learning algorithms has been developed since the advent of artificial neural networks in McCulloch and Pitts, 1943. To briefly organize the terminologies, artificial intelligence encompasses any computer technology that tries to implement human intelligence and includes all traditional ML and deep learning algorithms (Campesato 2020). ML utilizes data to train the model to educate itself for the output. Deep learning is the most specific term, that describes an approach that tries to imitate how the neurons work in the human brain (Campesato 2020). DNN is widely used in various fields today, and Reichstein et al. 2019 claims that deep learning methods are more suitable for solving problems for earth systems

compared to the traditional forms of ML. Deep learning contains multiple advantages over traditionally used ML algorithms, especially in combining the regression and feature extraction steps (Jainesch et al. 2021). While even more advanced deep learning methods incorporating statistical and/or more rigorous spatiotemporal information are available, the complexity of the model does not always provide improved results (Schultz et al. 2021). In this study, DNN, which is rather simple form of deep learning, is used to for both DSD retrieval and QPE purposes.

The biggest advantage that DNN provides is the ability to include nonlinear terms, and flexibility that are often lacking in previous deterministic or statistical approaches (Alzubaidi et al. 2021). DNN, like other ML, requires set of hyperparameters for optimal results. The process of choosing hyperparameters may often be difficult. The structure and design of the DNN model is consisted of choosing the model architecture and unifying input and output size and shape and choosing the parameters and activation functions (Fig. 9). DNN, including and often specified as multilayer perceptron in some literatures (e.g., Chen et al. 2020; Zhao et al. 2021), can be described as collection of links consisted of artificial neurons or perceptron. For each input, the output can be simply described in form of

$$y = f(wx + b) \qquad (21)$$

where y (e.g., rain rate, mass mean diameter, liquid water content) is the output, f the activation function, w the assigned weight, x the input variables (e.g., Z_h, Z_{dr}, K_{DP}), and b the bias term. While different activation functions are tested, the hyperbolic tangent (Tanh) function was used within the hidden layers to provide nonlinearity. The Tanh is in the form of a smooth nonlinear function and is often used for regression purposes. The rectified linear activation unit (ReLU) function is the most commonly used activation function for its efficiency. However, Tanh often provides

better results than ReLU for rather simple regression problems (Nwankpa et al. 2018; Szandala, 2020). Since the problem here is rather simple single point estimation, the Tanh function is used,

$$\text{Tanh} = (e^x - e^{-x}) / (e^x + e^{-x}) \tag{22}$$

where the x is the input (e.g., radar variables) matrix. The R estimation results display more errors when ReLU was used (Table 7). For other hyperparameters, the learning rate is set as 0.001 with multiplicative factor of learning rate of decay as 0.9 and step size of 5. The total number of epochs and batch size was fixed as 120 and 64, respectively. The loss is calculated in the form of mean squared error and are converted to RMSE.

Table 7. The R estimation results using linear (ReLU) and non-linear (Tanh) activation functions in percentage RMSE.

	Tanh	ReLU
RMSE (%)	1.04	2.83

The system design consists of standardization of the input data, regression, and output. In the standardization step, the inputted radar variables are standardized by removing the mean and scaling to the unit variance. Although DNN does not rely heavily on the distribution of input and/or output variables, the standardization process results in similar distribution of output variables and provide faster and more efficient optimization process. The estimation results display minimal difference due to input shape, size, distribution, and format. The regression was conducted for radar variables in dB scale, linear scale, and between the logarithm of the radar variables in linear units and logarithm of the estimators (Table 8). Here, Z_h and Z_{dr} were mainly used as input variables in linear units for single point estimations since 2DVD data are utilized. To match with the empirical method, the input estimators and radar variables were fitted after taking the logarithm

of both sides. While K_{DP} is also often used for QPE purposes, K_{DP} is excluded when using radar data because it does not have the same resolution variable compared to the previous two and may result in worse results than not including. Rain events are typically fairly distributed throughout the year, so the data were inputted in timely order. However, the order of the training data was randomized after every epoch (i.e., set of iterations) for efficient computations. The randomization process did not make much influence when 2DVD data was used, due to rather less complexity of problem with less observational errors. However, large differences were observed when randomization was not conducted for training radar data. Total fourteen different model architectures were trained with various number of hidden layers consisted of different number of nodes. The nodes in each layer were chosen as multiples of three or four, and the number of hidden layers vary from three to eight. Using the same algorithm, two different models, one for estimating physical parameters and the other rain rate, were trained for each error case. Although D_m and W are used together for DSD retrieval, the D_m is the ratio between the fourth and third, and W the third DSD moment. Thus, the results may differ when D_m is trained with or without W. Table 9 displays minimal difference in separating the two estimations when sufficient learning rate and epochs are provided.

Table 8. DNN results for D_m, W, and R estimations using PRD in dB and linear units for training

	Linear			Log (linear)			dB		
	D_m	W	R	D_m	W	R	D_m	W	R
RMSE	0.15	0.07	1.08	0.14	0.07	1.04	0.14	0.06	1.06

Table 9. The D_m estimation results using DNN for training only D_m and training both D_m and W.

	Only D_m	With W
RMSE (%)	0.14	0.14

For the selected hyperparameters and architecture, optimization process has to be adequately determined. The Adam algorithm is used as the optimizer (Kingma and Ba, 2015), which provides efficient optimization in the backpropagation step. Overall, the calculation of the output and optimization of the models can be simply put in four steps. First, the calculation of output y from the inputs x going through the hidden layers. Second, the cost function is computed in forms of mean squared error (RMSE) for given ground truth physical parameters and rain rate from 2DVD data. Third, the Adam algorithm, which is an iterative process utilizing the exponential moving average, is used in the backward propagation step to update the parameters in form of,

$$\theta_{t+1} = \theta_t - \frac{\alpha}{\sqrt{\hat{v}_t} + \varepsilon} \widehat{m}_t \qquad (23)$$

where $\widehat{m}_t$ bias-corrected first moment estimate, α the step size, $\sqrt{\hat{v}_t}$ bias-corrected second raw moment estimate, ε small hyperparameter preventing division of 0 (Kingma and Ba, 2015). Lastly, the weights are iteratively updated until optimal solution is reached. After the training is completed, RMSE of training, validation, and testing datasets for epochs that reduced RMSE compared to the previous epoch are saved. The architecture and epoch displaying lowest validation RMSE were further selected for testing.

In addition to the advantageous properties of DNN described previously, it can relatively include additional input/output variables, and spatiotemporal information (Alzubaidi et al. 2021). In addition, the different weights, and bias function helps find optimal solutions when various observational errors exist in the input/output variables. Similar to the empirical formulas in the previous section, the DNN were trained for each data containing different observational errors.

DNN requires precautions when choosing the training data. For example, if the model is trained using stratiform rain only, it will have difficulties predicting higher values of estimators for

convective rain. This is because convective rain contains both small and large rain rates while light rain dominates in stratiform rain. The usage of even the most updated machine learning does not always provide better results over conventional statistical methods in all situations and areas of research due to ML issues such as data preprocessing, detrending, computational complexity and overfitting (Makridakis et al., 2018). In fact, statistical methods showed better results in cases when abundant prior information is known about the topic, and input variables were limited and established (Rajula et al., 2020). Thus, both the quantity and quality of the training data matters heavily for DNN to perform well. As shown in Fig. 10, the nonlinear terms of DNN are evident in both linear and logarithmic domain. However, in linear domain (Fig 10a), the DNN's R estimations are curved flat from about 60 mm hr^{-1} due to lack of representation of high R values in the training data. This may imply that DNN may not be suitable for estimating unusual and record-breaking rain events. Further representation of larger rain rate values is required.
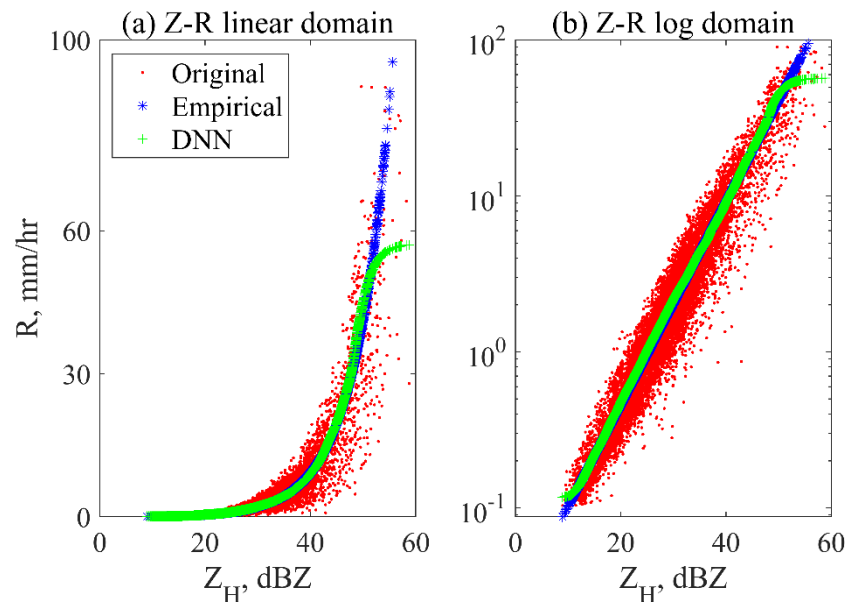
Fig. 10. The rain estimations from only radar reflectivity using power law and deep neural network in (a) linear and (b) logarithmic domains.

In order to choose the appropriate hyperparameters and choose/test the appropriate form of input data for the DNN, various testing was conducted. The PRD data in dB and linear units, different activation functions (Tanh vs. ReLU), and testing and training on two different data (stratiform and convective rain) were conducted. Several strengths, weaknesses, and potential for improvements of DNN were located.

1. Influence of input type, shape, size, and form

   In order to locate the nonlinearity of outputs using DNN, the Z-R relationship was initially tested. As shown in Fig. 10, the DNN displays nonlinear ends and wavy ends, explicitly displaying the nonlinear outputs. In addition, the lack of large values and below 0.1 mm hr^{-1} in the training data resulted in lack of estimations for higher rain rate and near zero points. Next, three different input forms of radar variables were conducted, in linear units, logarithm of both input variables and estimators, and dB unit radar variables (Table 8). As mentioned previously, all three forms did not make a large influence on the D_m, W and/or R estimations. The absolute RMSE was 0.15, 0.14,0.14 for D_m, 0.07,0.07,0.06 for W, and 1.08,1.04,1.06 for R estimations using linear, logarithm of linear, and dB units of input radar variables. These results indicate further uses of various distributions of input and output variables can be used, showing strengths compared to the previously used statistical or deterministic approaches. It is common for the empirical formula to conduct the fitting between the logarithmic of the PRD in linear units, and the logarithmic of physical parameters or rain rate. However, some statistical methods, such as the Bayesian retrieval (Cao et al. 2008) simply uses the PRD in dB units for the retrieval process. Thus, both forms of input data are trained and tested. While no significant differences are noticed, the

regression was conducted identically as the empirical method, as the logarithm of both input and output variables and parameters.

2. Two different training and testing data

For QPE purposes, stratiform and convective region are often separated. The stratiform and convective region display completely different physical mechanisms in the growth of clouds resulting in different characteristics. Here, the data was divided into stratiform rain and convective rain based on the Bayesian classification (Bukovcic et al. 2014). Based on the classification results, the 2DVD data was divided for training and testing data. First, DNN trained from convective rain was tested with stratiform rain. While the errors increased compared to training with stratiform or combination of convective and stratiform rain, the results were fairly accurate with RMSE of 14.9% (Fig. 11). However, when the DNN was trained with stratiform rain and tested on convective rain, the results deteriorated further, with RMSE of 124.4% (Fig. 11). This is due to the lack of higher rain rate values in stratiform rain data. This further emphasizes the need for similar PDF and values of training and testing data for the DNN. Similar result is shown in figure 8, due to the distribution of the training data, the model lacks the ability to estimate R above 60 and below 0.1 mm hr^{-1}.
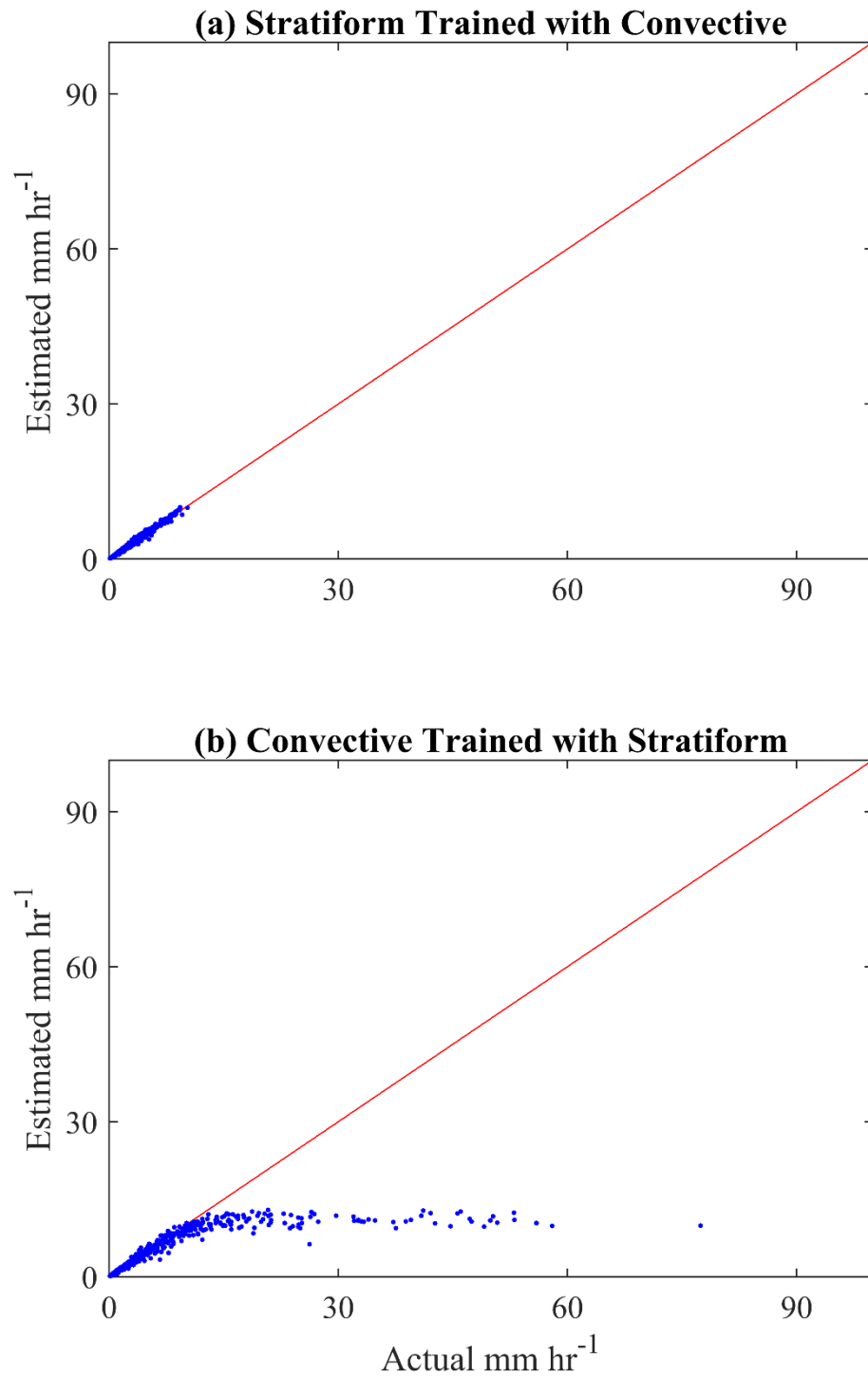
Fig. 11. The rain estimations for convective rain cases trained with convective (top) and stratiform (bottom) events.

5. Results from two dimensional video disdrometer data

The three methods (physics-based inversion, empirical formula, and DNN) were compared and evaluated using the ground truth 2DVD data. The three variables (D_m, W, and R) were estimated for two temporal domains (instantaneous and rain-event-average) and three error sources (perfect, adding measurement, and with model errors). The perfect error represents that no additional errors were added to the parametrized operators, and only fitting errors from each method exist. The adding measurement error randomly assigns gaussian error with standard deviation of 1 dBZ for Z_H and 0.2 dB for Z_{DR}. Model error category utilizes the variables that were numerically integrated from 2DVD observed DSD data and numerical integration with T-matrix calculated scattering amplitudes for S-band radar; errors come from difference between 2DVD observations and physics-based models. The error distributions were illustrated as psuedocolor, scatter, and box plots for the three variables, three methods, and three error sources. The relative bias and RMSE were also calculated.

5.1 Instantaneous domain

The estimation errors of D_m, W, and R were calculated by substituting 2DVD observed truth from the estimates using the physics-based inversion (physics hereafter), empirical formula (empirical hereafter), and DNN methods. The figures 12-14 display the psuedocolor plots each for the three types of errors, figure 15 and figure 16 the error distributions categorized into the three error sources, perfect, adding measurement, and with model errors each using scatter and box plots in instantaneous domain. It is noted that numbers of 2DVD testing data vary depending on the error sources, 11,577-13,037 minutes. The pseudocolor plots may indirectly provide information

regarding the dependence of each estimator on Z_H and Z_{DR}. The one-one plot and box plots explicitly display the outlying points and/or the bias of each method for the observational errors. In the perfect error category (Figs. 12, 15 and 16 a−c), estimation errors of the three variables in interquartile range (i.e., between 25% and 75%) are nearly zero for the physics and DNN methods. Relatively, errors in the empirical method are meaningfully larger in all three variables; in D_m, the interquartile range is distributed in the negative errors; however, outliers are spread in the positive errors (Fig. 16 a). In W and R (Figs. 15 and 16 b and c), the interquartile range of the empirical method is situated near zero; however, outliers are widely dispersed in the negative errors. This larger error in the empirical method is due to the perfect error category utilizing parameterized operators derived in polynomial forms, while power law forms are used for the empirical formulas. Nevertheless, all methods show small errors for all three estimators in perfect error category. The pseudocolor plots display similar distribution for physics based and DNN methods (Fig. 12).
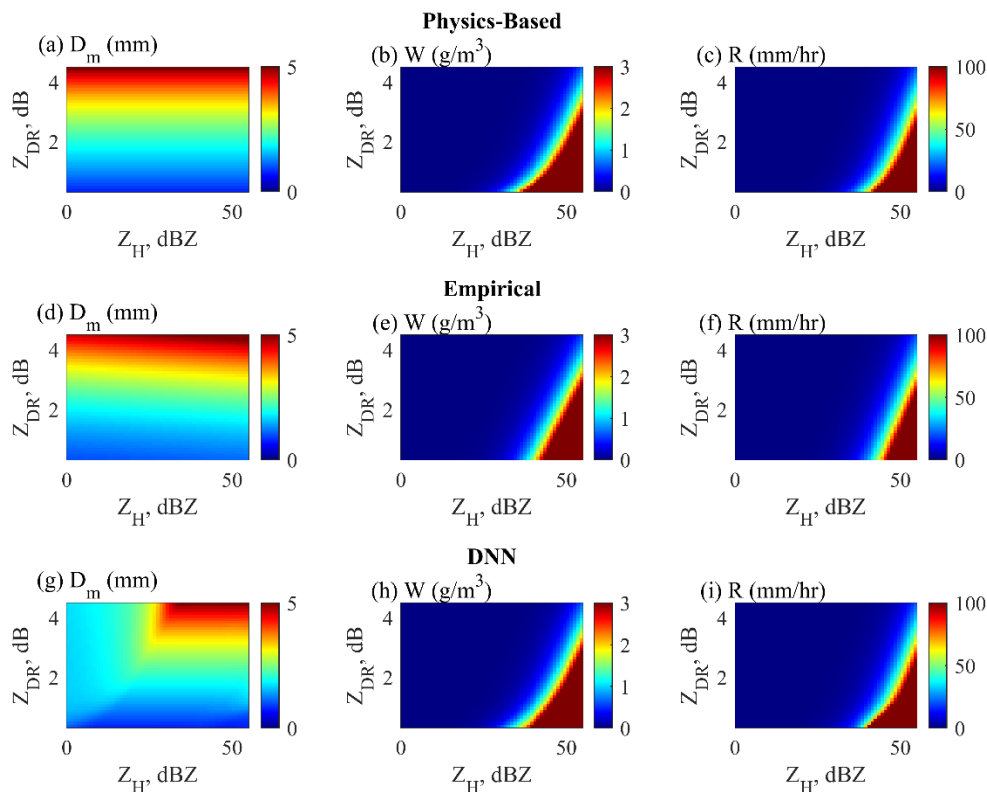
Fig. 12. Psuedocolor plots displaying the distribution of the estimation results for D_m, W, and R given perfect error case using (a–c) physics-based inversion, (d–f) empirical, and (g–i) DNN methods.

In adding measurement errors compared to the perfect error category, estimation errors increase for all methods and variables; the maximum error values increase up to 5 times (Figs. 13, and 15 and 16 d–f). The interquartile range appears thicker in D_m (Figs. 15 and 16 d) and remain thin near zero in W and R for all methods (Figs. 15 and 16 e and f). The outliers are spread in both positive and negative errors with small bias. In the with model error category, the range of outliers increase in D_m (Fig. 15 and 16 g) and rather decrease in W and R (Figs. 15 and 16 h–i) as compared to values in the adding measurement error category. The errors for the three estimators increased, displaying some clear differences in performance between the three methods. The physics method

deteriorated heavily, the interquartile range of D_m is distributed from -0.4 to -0.6 mm, showing a very large negative bias, with 0.2-0.3 g m^{-3} interquartile range for W, and 2-3 mm hr^{-1} R with positive bias. The empirical method represents an error outlier distributed to the positive value in D_m and the negative in W and R. While the range of outliers increased for DNN in both positive and negative regions, the interquartile range and the median stayed near zero. Summing up, for the three methods, three variables, and three error sources, DNN shows the smallest residuals with near-zero bias even in cases inclusion of measurement or model errors. From figures 13 and 14, empirical (d-f) and DNN (g−i) utilizes Z_H more for D_m estimation compared to perfect error category as observational errors were included. For W and R estimations, empirical and DNN methods display rather narrow regions of higher estimator values compared to physics-based method (a−c), as observational errors were included.
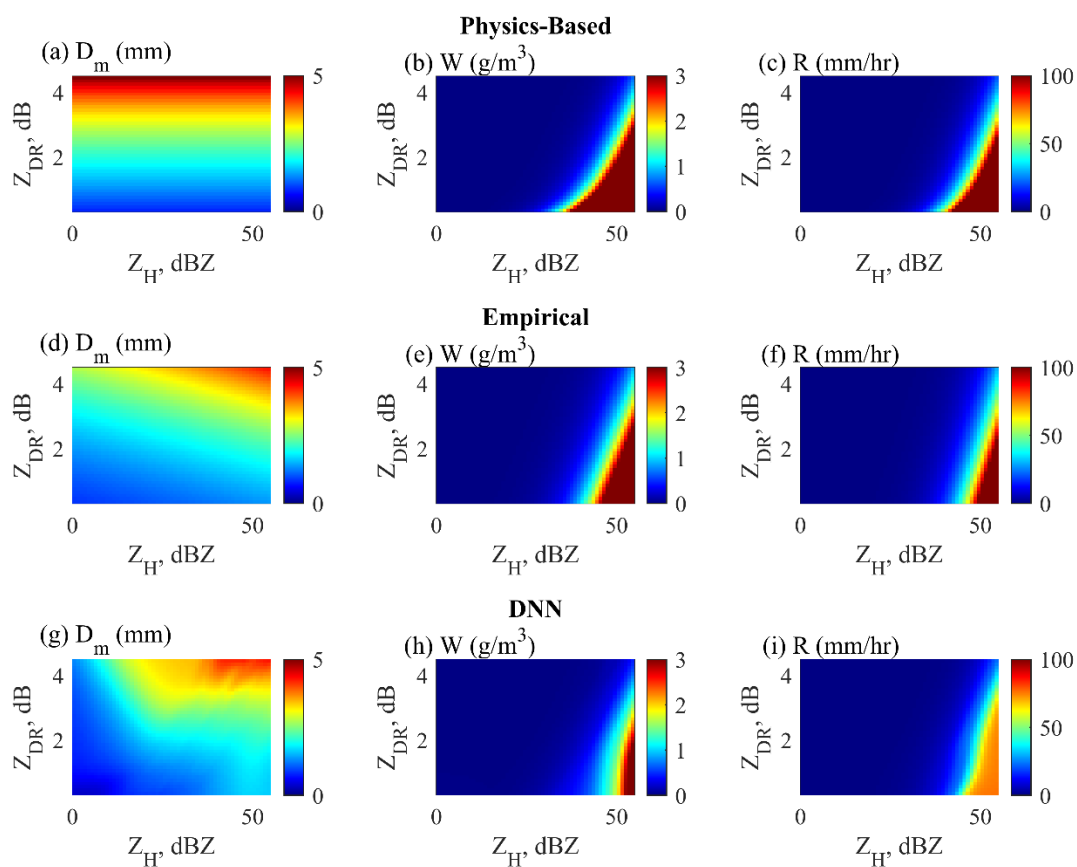
Fig. 13. Same as Fig. 12 except for measurement error case.
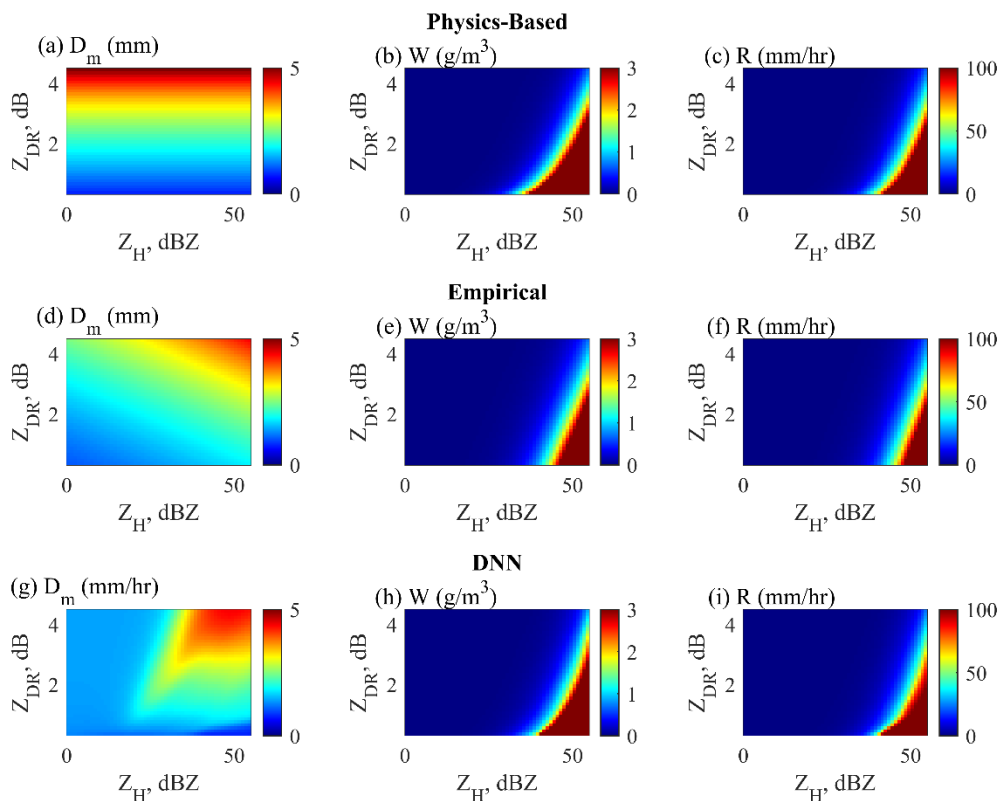
Fig. 14. Same as Fig. 12 except for model error case.

In the same way, the relative bias and RMSE of the parameter estimates for the three variables, the three methods, and the three error sources were shown in Table 10. In the table, the error values are grouped according to the error sources, (a) perfect error, (b) adding measurement error, and (c) with model error. In the perfect error category (Table 10a), using the physics and DNN methods, bias and RMSE were found to be less than 1% in all three variables. By contrast, there are large errors in the empirical method: the bias increases to 3.6% and the RMSE increases to 17.1% in W. As adding measurement errors, bias and RMSE increase significantly for all variables and methods (Table 10b). Overall, the errors of the three methods are analogous for D_m. For W and R, however, the biases are around 1% in DNN and 5-9% in the other two methods. The RMSE values are so

large that the physical method shows about 75%, and the empirical and DNN methods show close to 60%. When model errors are added (Table 10c), the errors increase largely in the physics method compared to when measurement errors are added but decrease in the empirical and DNN methods with substantial reduction in bias. Compared with the empirical method, the DNN method shows smaller errors in general. Taken together, the results from Table 10 indicate that the physical method shows large errors in the three variables, with DNN displaying smallest bias and RMSE especially when adding model errors. Summing up, for the three methods, three variables, and three error sources, DNN shows the smallest absolute error value with near-zero bias even in cases of observational errors.
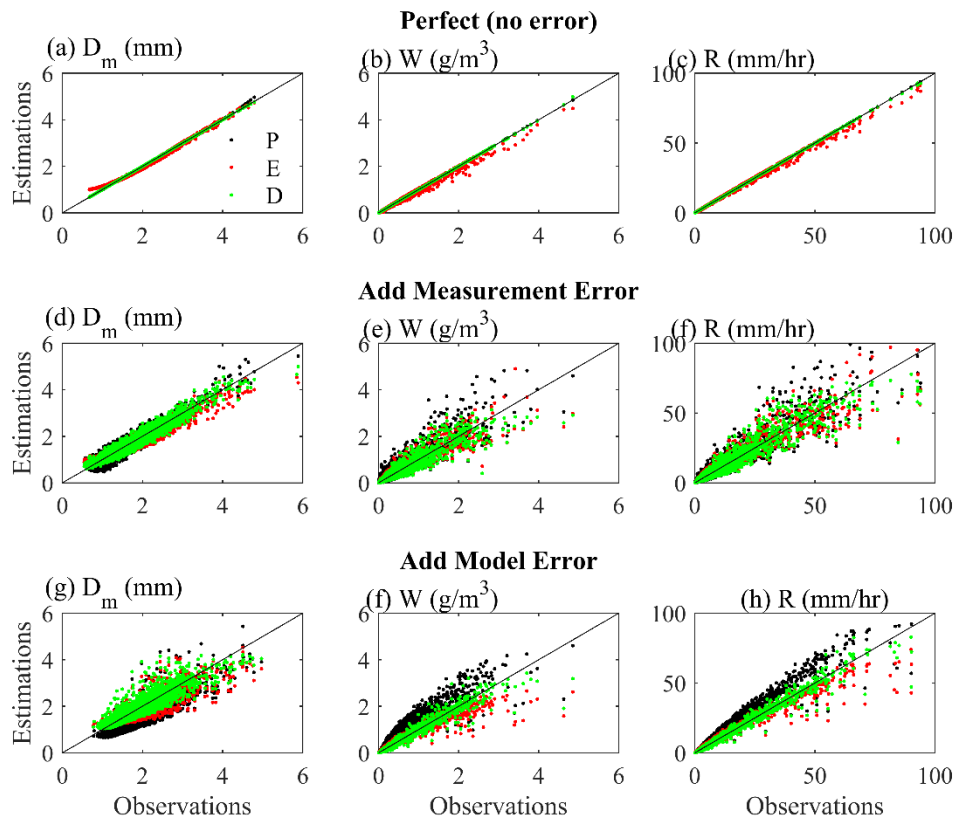
Fig. 15. Scatter plot displaying the estimation results of mass-/volume-weighted diameter (Dm), liquid water content (W), and rain rate (R) using physics-based inversion (P), empirical formula (E), and DNN (D) methods in instantaneous domain.
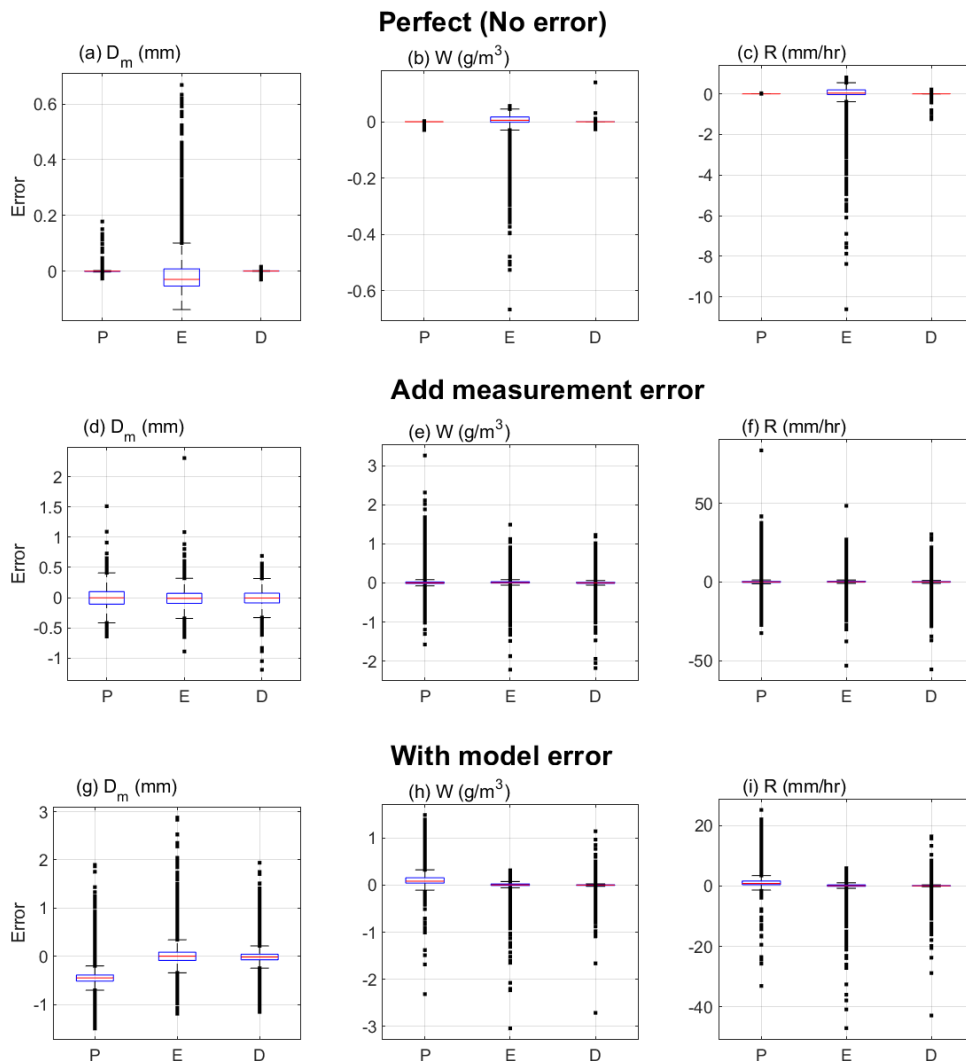
Fig. 16. Box plot of the error distributions of mass-/volume-weighted diameter (D_m), liquid water content (W), and rain rate (R) for the physics-based inversion (P), empirical formula (E), and DNN (D) methods in instantaneous domain. There are three error sources, (a–c) perfect, (d–f) adding measurement, and (g–i) with model errors to instantaneous two-dimensional video disdrometer (2DVD) data for the period 2006–2017. Numbers of instantaneous 2DVD data vary depending on the error sources, 11,577–13,037 minutes. In each box, lower and upper boundaries denote interquartile range (25% and 75%, respectively), line inside box median, lower and upper error lines 1.5 interquartile range, and dots outlier values beyond the 1.5 interquartile range. Unit for D_m is mm, W g m^{-2}, and R mm hr^{-1}. The y-axis tick marks are adjusted accordingly.

Table 10. The bias and RMSE of the error estimation for the three variables (D_m, W, and R) and three methods—physics (P), empirical (E), and DNN (D)—in instantaneous domain according to the three error sources, (a) perfect error, (b) adding measurement error, and (c) with model error. The unit is %.

	D_m			W			R		
	P	E	D	P	E	D	P	E	D
Bias	-0.1	0.5	0.0	0.0	3.6	-0.1	0.0	1.8	-0.1
RMSE	0.4	4.4	0.1	0.3	17.1	0.9	0.1	11.3	0.9

(b) Adding measurement error

	D_m			W			R		
	P	E	D	P	E	D	P	E	D
Bias	-0.1	-0.7	-0.5	9.1	8.3	-1.1	6.5	5.6	1.2
RMSE	8.1	8.7	10.1	77.0	59.0	57.3	74.4	60.4	58.5

(c) With model error

	D_m			W			R		
	P	E	D	P	E	D	P	E	D
Bias	-27.3	0.5	-0.4	70.8	1.0	-0.9	37.3	0.8	-0.3
RMSE	29.1	11.8	9.5	111.4	50.6	35.1	69.1	36.9	25.8

5.2 Event average domain

The previous analysis was repeated by summing each continuous rain period for at least 20 minutes, including up to ten-minute interruptions, from the instantaneous 2DVD data (Figs. 17 and 18). There are 127 rain-event-average cases for the analysis 2DVD data. Since rainy periods vary from 22 to 950 minutes, there are differences of error distributions between instantaneous and rain-event-average domain. For the perfect error category (Figs. 17 and 18 a-c), the physics and DNN methods show nearly zero error for the three variables; the empirical method shows minor errors. By adding measurement error (Figs. 17 and 18 d-f), the errors slightly increase for the three methods and variables. The interquartile ranges of the error are located around zero, and the median value is also near zero. Since gaussian error were added to the input variables, the averaging process reduced errors significantly when rain-event-averaged values were compared.

Overall, it is difficult to determine which of the three methods is superior. In the category where model errors are involved, the difference among the three methods is noticeable (Figs. 17 and 18 g-i). This is evident in the physics method that the median value of the error is 0.45 mm in D_m, -0.11 g m^{-3} in W, and -0.12 mm hr^{-1} in rain rate. In the DNN method, the interquartile range of W and R lies near zero, indicating very accurate estimation (Figs. 17 and 18 h and i).

Table 11. Same as Table 10 except for rain-event-average domain.

(a) Perfect error

	D_m			W			R		
	P	E	D	P	E	D	P	E	D
Bias (%)	-0.1	-0.2	-0.0	-0.0	1.1	-0.1	0.0	0.4	-0.1
RMSE (%)	0.2	2.9	0.1	0.2	9.7	0.3	0.0	6.2	0.3

(b) Adding measurement error

	D_m			W			R		
	P	E	D	P	E	D	P	E	D
Bias (%)	-0.2	-0.5	-0.7	8.3	5.7	-1.8	6.1	4.1	1.1
RMSE (%)	1.7	3.6	3.1	17.1	13.5	12.4	15.7	11.6	10.9

(c) With model error

	D_m			W			R		
	P	E	D	P	E	D	P	E	D
Bias (%)	-26.6	0.9	-0.6	59.8	-3.5	-1.6	32.1	-2.4	-1.0
RMSE (%)	27.0	5.7	4.0	71.7	26.4	14.2	40.5	19.6	10.9

Table 11 displays the relative bias and RMSE estimated for the three variables, methods, and error sources using 127 cases in rain-event-average domain. For the perfect error category, the physics and DNN methods produce almost perfect results for all three variables, but the empirical method produces an error of 9.7% in W and 6.2% in R estimation (Table 11a). For adding measurement error category, there is no significant difference between the three methods in D_m estimation (Table 11b). DNN method is somewhat superior in estimating W and R, but there is no obvious difference between the three methods. When model errors are involved, there is a large

difference in bias and RMSE between methods (Table 11c). In the physics method, the absolute value of the bias and RMSE error was 20% or more in all three variables. In particular, a large error in the bias is noteworthy. In the empirical method, errors decrease significantly compared to the physics method, but the RMSE error is 26.4% in W and 19.6% in R estimation. The error is greatly reduced in DNN method; as compared to the result of empirical method, it is about half.
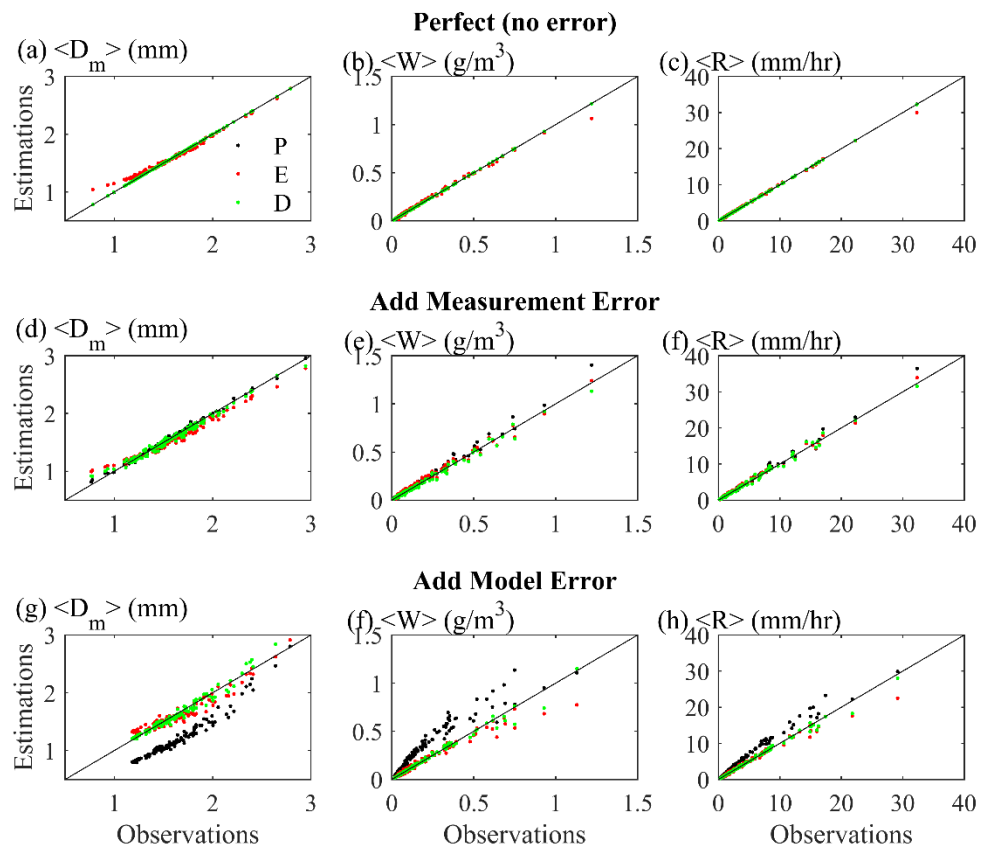
Fig. 17. Same as Fig. 15 except for rain-event average domain. Number of rain-event average case are 127.

Perfect (no error)

Add measurement error

With model error
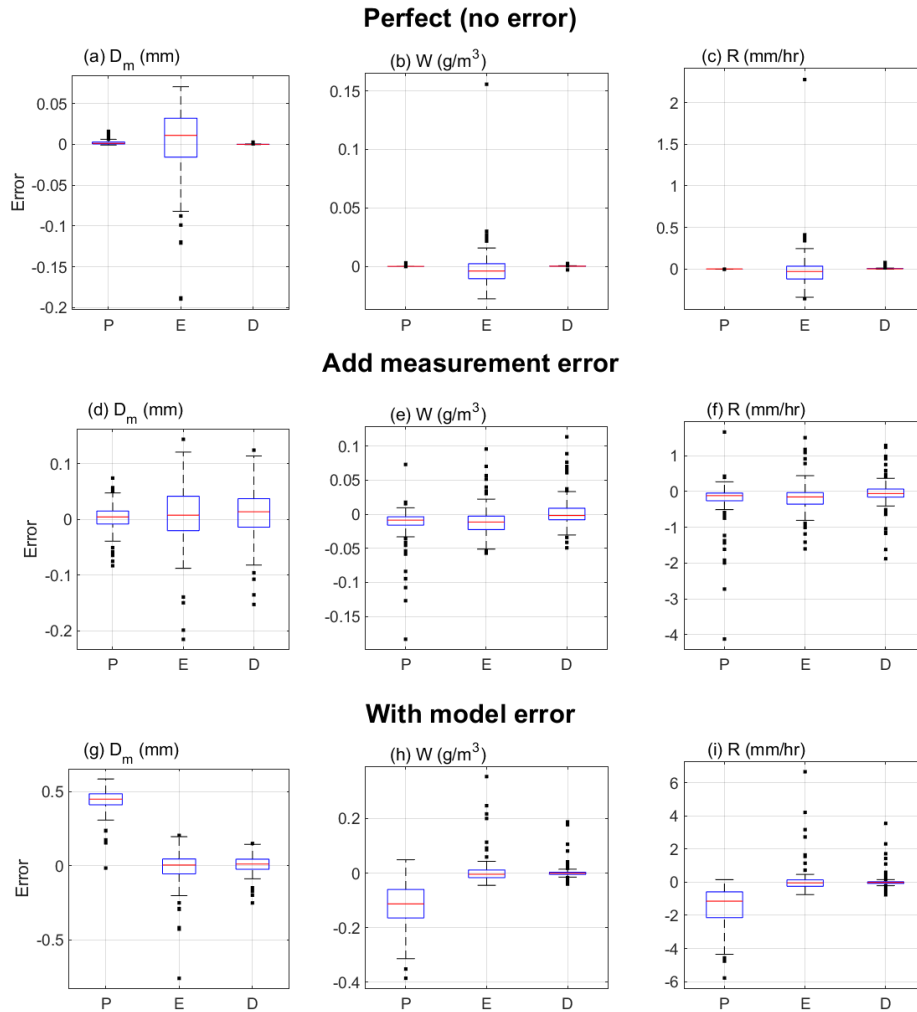
Fig. 18. Same as Fig. 16 except for rain-event-average domain. Numbers of rain-event-average case are 127.

5.3 Additional variable and information

One advantage of DNN is the ability to include additional input and/or output variables relatively easily. Using this ability, additional spatial and/or temporal information can be incorporated for the estimations. Here, inclusion of K_{DP} and 20-minute temporal information are trained and tested using 2DVD data. As mentioned previously, K_{DP} is widely used for QPE for

heavy rain and cases containing hail by combining Z_h and K_{DP} in empirical formulas. Including

K_{DP} lowered RMSE for about 5% when model errors exist, with slightly higher bias compared to

only using two polarimetric variables (Table 12 and figure 19). Next, the 20-minute temporal

information were included. The radar variables from 20 minute prior to the corresponding time

(i.e. t-19 to t for corresponding time t) were used. Incorporating 20-minute prior information

reduced the RMSE for about 10%, while bias remained similar, or slightly higher compared to

single point estimations (Table 13 and figure 20).

Table 12. Comparison of R estimations for with model error category including K_{dp}.

	Perfect	Measurement	Model
Bias (%)	0.1	5.2	-1.9
RMSE (%)	1.1	58.5	21.9
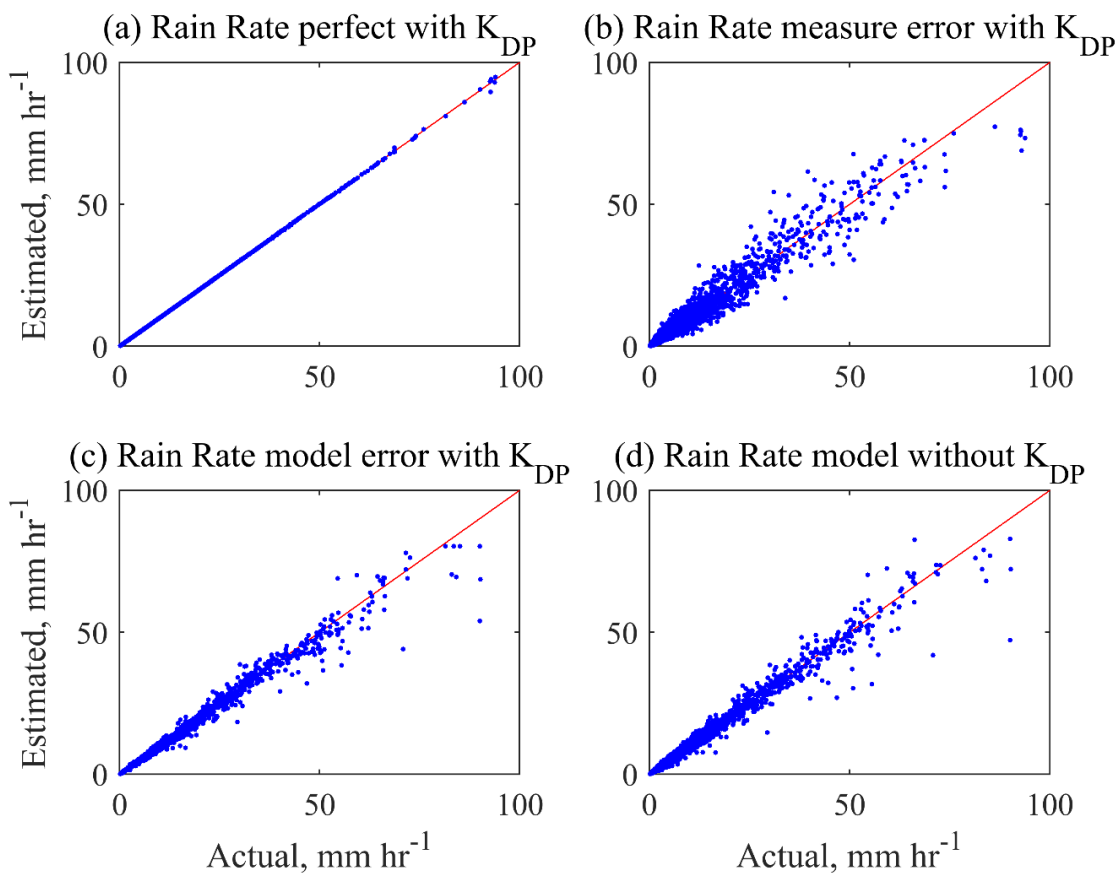
Fig. 19. Scatter plot of rain estimation for perfect (a), measurement error (b), model error (c) category after including K_{DP} for rain estimation comparing with the rain estimation for model error category without K_{DP}.

Although notable improvements are shown when including additional polarimetric variable, K_{DP}, and temporal information of fixed 20-minutes, verification on real radar data are not conducted further. This is because K_{DP} are often prone to contamination when using radar data, and other polarimetric variables are not appropriate to include in this single-point estimations conducted in this research; ρ_{hv} is not suitable for DSD retrieval or QPE purposes due to small variations in its values, and Φ_{DP} is often used for entire ray of radar data. Note that K_{DP} that is numerically integrated from 2DVD observed DSD are often less contaminated by large errors.

Thus, these results indicate that inclusion of additional polarimetric variables, if properly used, can assist in estimations. While temporal information may also help improve estimation results, the DNN model used in this research requires fixed input size, and have difficulties in including varying temporal resolution and storm lengths when using real radar data.

Table 13. The results using twenty-minute temporal information for model error category.

(a) D_m

	15	20	30
Bias (%)	-1.2	0.1	-0.7
RMSE (%)	6.2	5.6	5.2

(b) W

	15	20	30
Bias (%)	-0.8	0.5	-0.5
RMSE (%)	26.2	24.4	20.1

(c) R

	15	20	30
Bias (%)	-0.5	1.7	-0.5
RMSE (%)	18.6	15.8	12.3
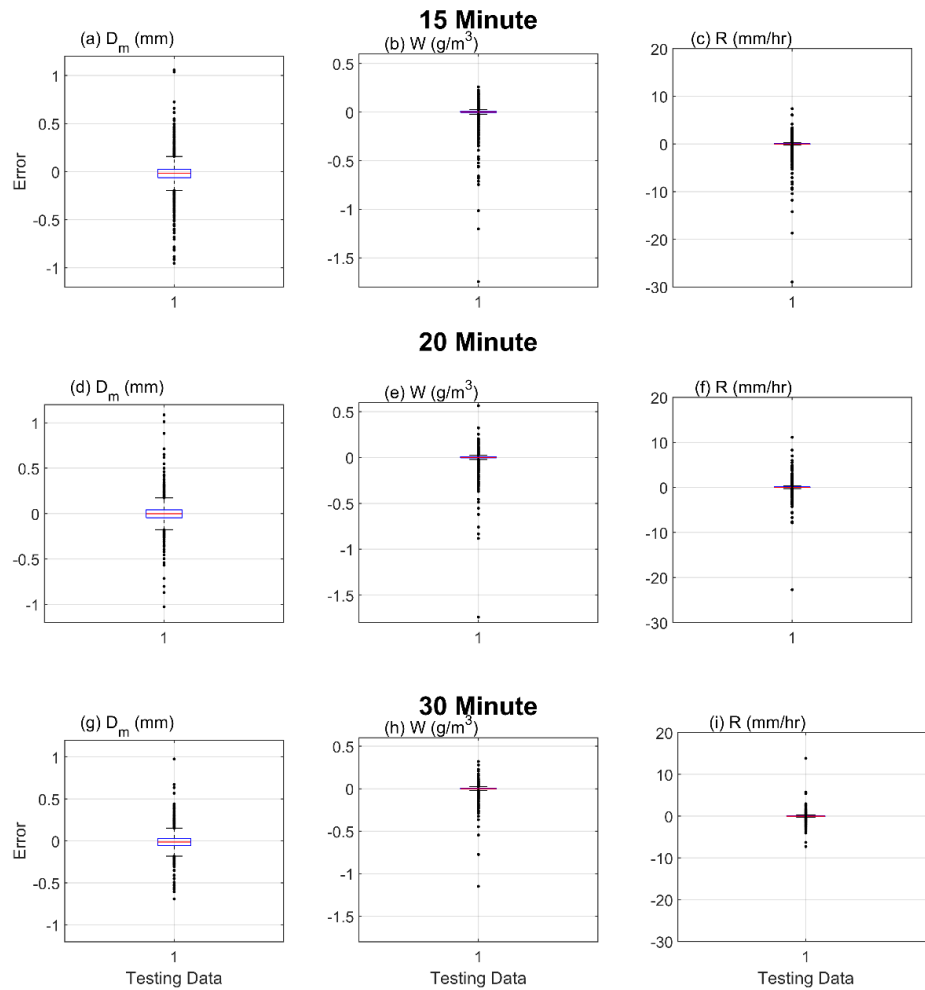
Fig 20. Scatter plot of D_m, W, and R estimation when fifteen, twenty, and thirty minute temporal information are included for model error category.

6. Verification on radar data

As seen in the previous section, the performance of the physics-based inversion retrieval degraded greatly when model errors existed. Consequently, the physics method is not used in the following analysis. Here, previously developed empirical and DNN methods based on 2DVD data

were applied to the real radar data. Then, both empirical and DNN methods were trained and evaluated directly using radar observation data.

6.1 Model training with 2DVD data

Aforementioned trained models using 2DVD data were applied to radar data. Due to differences in observation data (S-band radar and 2DVD), there is inherent bias between the training (2DVD) and testing (radar) data, which varies depending on the distance and elevation (Tokay et al. 2020). In order to avoid confusion with the percentage bias calculated as evaluation metrics of the estimators, the adjustments between the two different datasets will be written as BC. Table 3 displays the estimation results for the three variables with and without BC. For all three estimators, large biases are noticed in the estimation results without BC. Here, the BC was -3.0 dBZ for Z_H and 0.12 dB for Z_{DR} with the radar observations being smaller than the 2DVD (Fig. 21). The RMSE using DNN for before and after BC does not show much difference for all three estimators with 19.7,148.3,120.8% without BC, and 22.0,147.9,163.1% with BC for Dm, W, and R, respectively (Table 14). The bias reduced significantly, from 20 to 10% for D_m and -48.6, -42.7% to -5.2 and -0.2% for W and R estimation, respectively. Comparing with the empirical method, the bias for D_m was almost half of that of DNN, with similar RMSE. For W and R estimations, the bias and RMSE were similar (Table 14). The similar or increased RMSE values after BC are probably induced from outliers, which are minimally affected from the adjustments of the two datasets. In addition, due to the large mean difference, large values from radar observations may have increased even more due to the BC, resulting in higher RMSE than prior to BC. Note that RMSE is often affected by small number of large errors and may not represent overall deterioration or improvement.

Comparison of radar variables between 2DVD and Radar
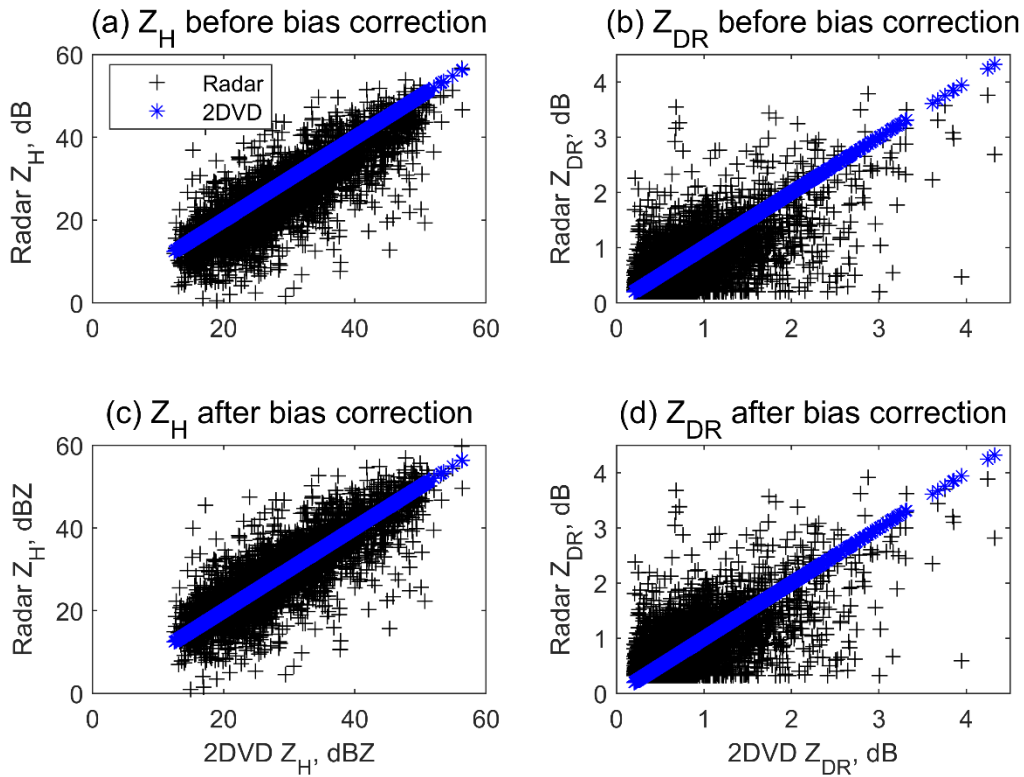
Fig. 21. Scatter plot comparing the polarimetric variables, Z_H and Z_{DR} distribution based on 2DVD and radar observations for corresponding days.

Table 14. The bias, root-mean-square-error (RMSE), and bias factor of the error estimation from radar data, using 2DVD trained empirical (E) and DNN (D) methods. The three variables (D_m, W, and R) without and with bias correction (w/o BC and w/ BC, respectively) are shown. Unit is %.

	D_m				W				R			
	w/o BC		w/ BC		w/o BC		w/ BC		w/o BC		w/ BC	
	E	D	E	D	E	D	E	D	E	D	E	D
Bias (%)	4.5	4.3	5.1	10.9	-44.9	-48.6	-4.3	-5.2	-39.6	-42.7	2.6	-0.2
RMSE (%)	19.4	19.7	16.4	22.0	84.4	92.1	121.8	148.3	116.4	120.8	147.9	163.1

Total bias factor	1.0	1.0	1.1	1.1	0.6	0.5	1.0	0.9	0.6	0.6	1.0	1.0

It is noticed that large increase of errors was noticed for both empirical and DNN methods when tested on radar data, but the overall bias/total bias factor may be reduced by adjusting the mean difference (BC) in the two different datasets. The bias factor for empirical method shows similar results with previous publications (Brandes et al. 2002). Large number of outlying points were noticed, due to both observational errors and additional physical reasons (Figs 22–24). Additional errors in instantaneous domain were expected, due to increased amount of observational errors and sources of contamination that often occurs in radar data. Note that the mean difference between the ground and radar observation differs heavily based on the distance between the two and may require accurate BC for each location of various distances for accurate estimations (Tokay et al. 2020). Thus, this implies that training will be required for each distance away from the radar with adjusted bias.
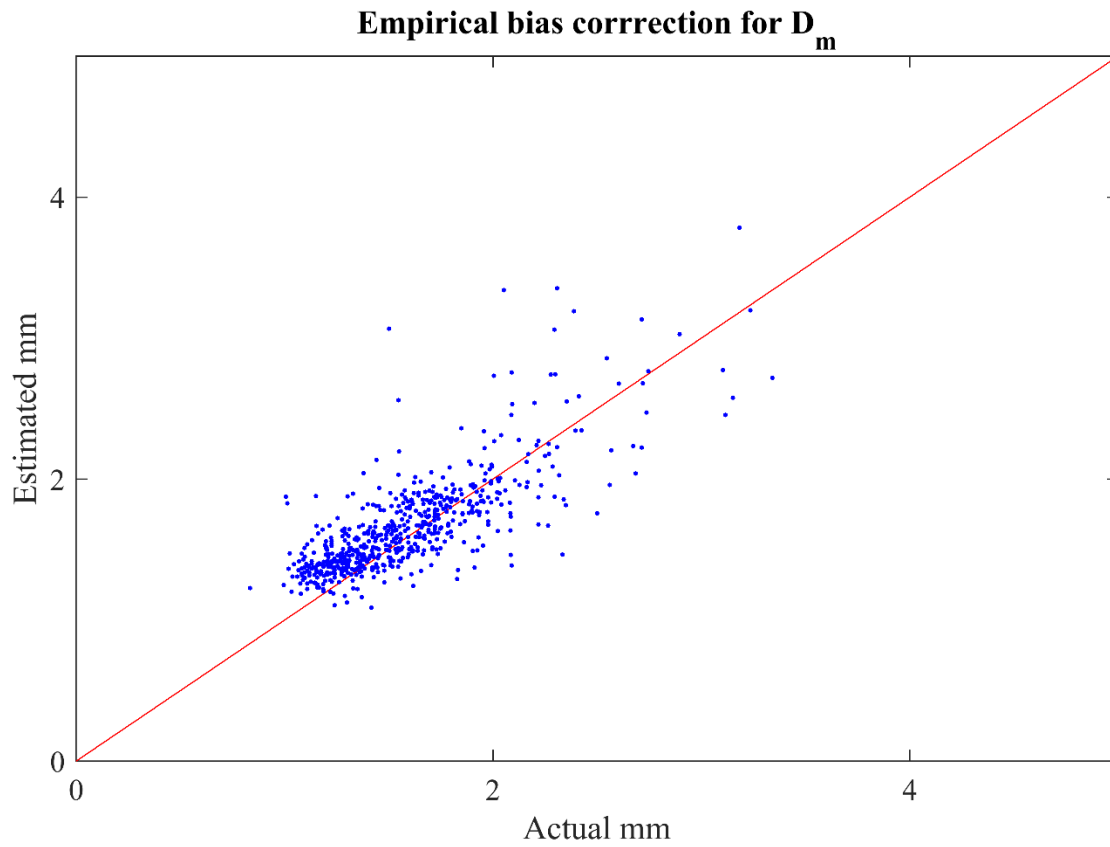
Fig. 22. The D_m estimation result for 2DVD trained empirical method tested on radar data.
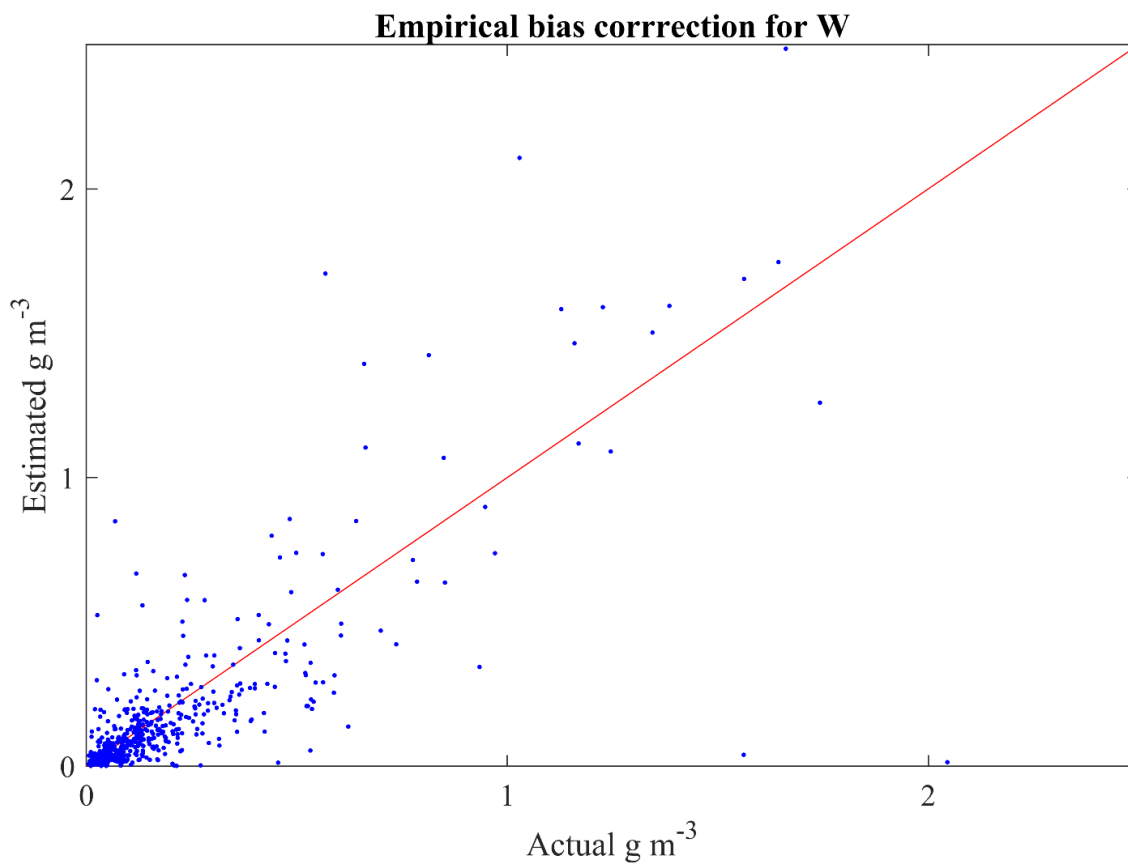
Fig. 23. Same as figure 22, excpet for W estimation.
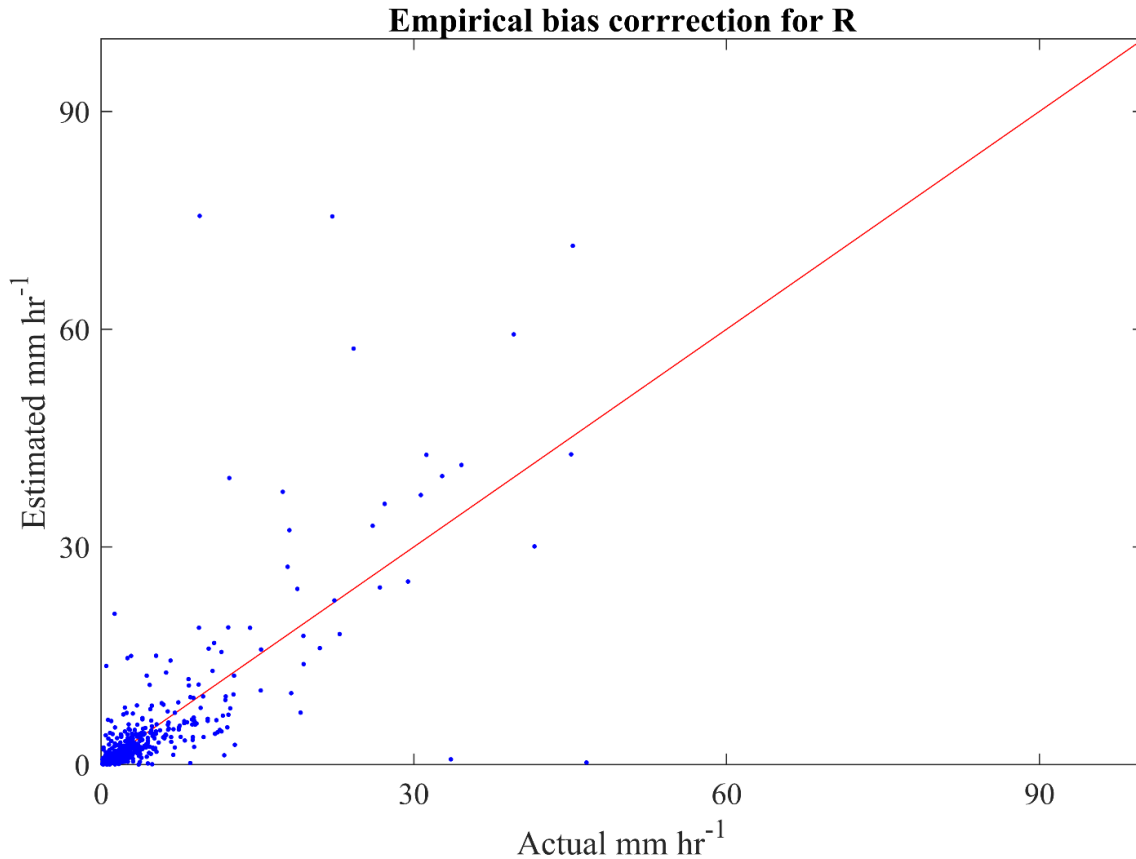
Fig. 24. Same as figure 22, except for R estimation.

6.2 Data Augmentation

Estimation results of D_m, W, and R using radar data only were evaluated comparing with the ground-truth (2DVD) values; 80% of radar data were used for training, 10% for validation, and the remaining 10% for testing. The distribution of Dm, W, and R showed less than 10 points in the higher values of estimators, which hinders proper estimation of those values that lack representations in the training data (Figs. 25−27). Due to the lack of data points in the radar data for training, data augmentation techniques were used. Data augmentation increases the amount of data by clustering additional points around the original data with very small changes. In addition

to increasing training data, data augmentation also helps form invariant predictions (Cui et al. 2014). Data augmentation is typically conducted by uniformly adding gaussian distributed random noise (Xu et al. 2016). Applications or examples of data augmentation for DSD retrieval or QPE purposes using radar data are not abundant, and the following form of equation was used (Kim et al. 2020; Mikolajczyk and Grochowski 2018),

$$x' = x + C \times \sigma \times N$$

where x is the original data, N is the gaussian distributed random number, σ standard deviation of 1, and C is a constant term set as 10^{-7}. The constant is set as 10^{-7} because the C should be small enough to not increase any errors in the data, while sufficient amount of change should be included to avoid truncation and overfitting issues. Other methods such as modifying class weights to put more weighting for the less represented range may also be possible. However, only 26 points exist for rain rate over 50 mm hr^{-1} compared to 4043 points below 5 mm hr^{-1}. Similar ratio was shown for the 2DVD dataset, with a lot less points for higher rain rate. This implies that the absolute number of data points are also essential in addition to the ratios between ranges.
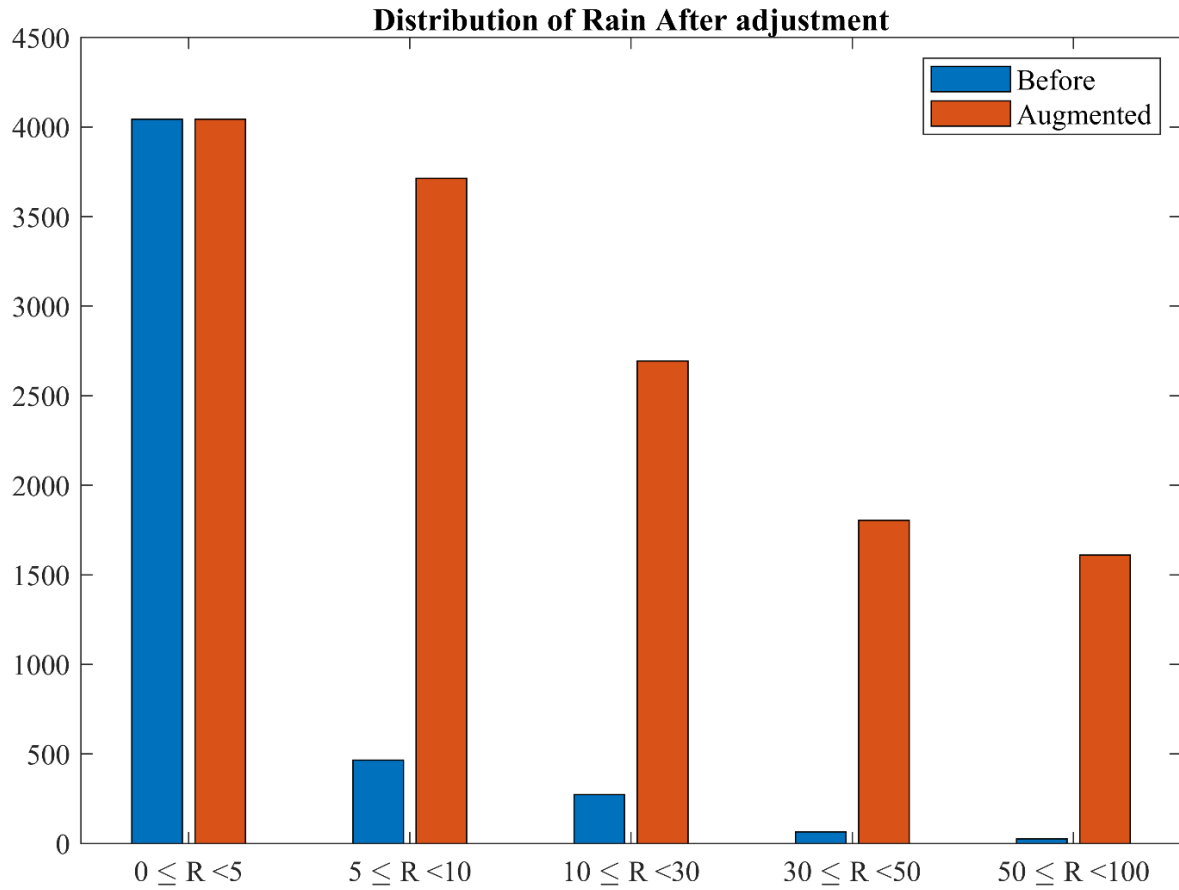
Fig. 25. Bar plot displaying the number of training data for each range of rain rate values. The blue bar shows the original data, and the yellow after data augmentation. The rain rate is in units of mm hr^{-1}.
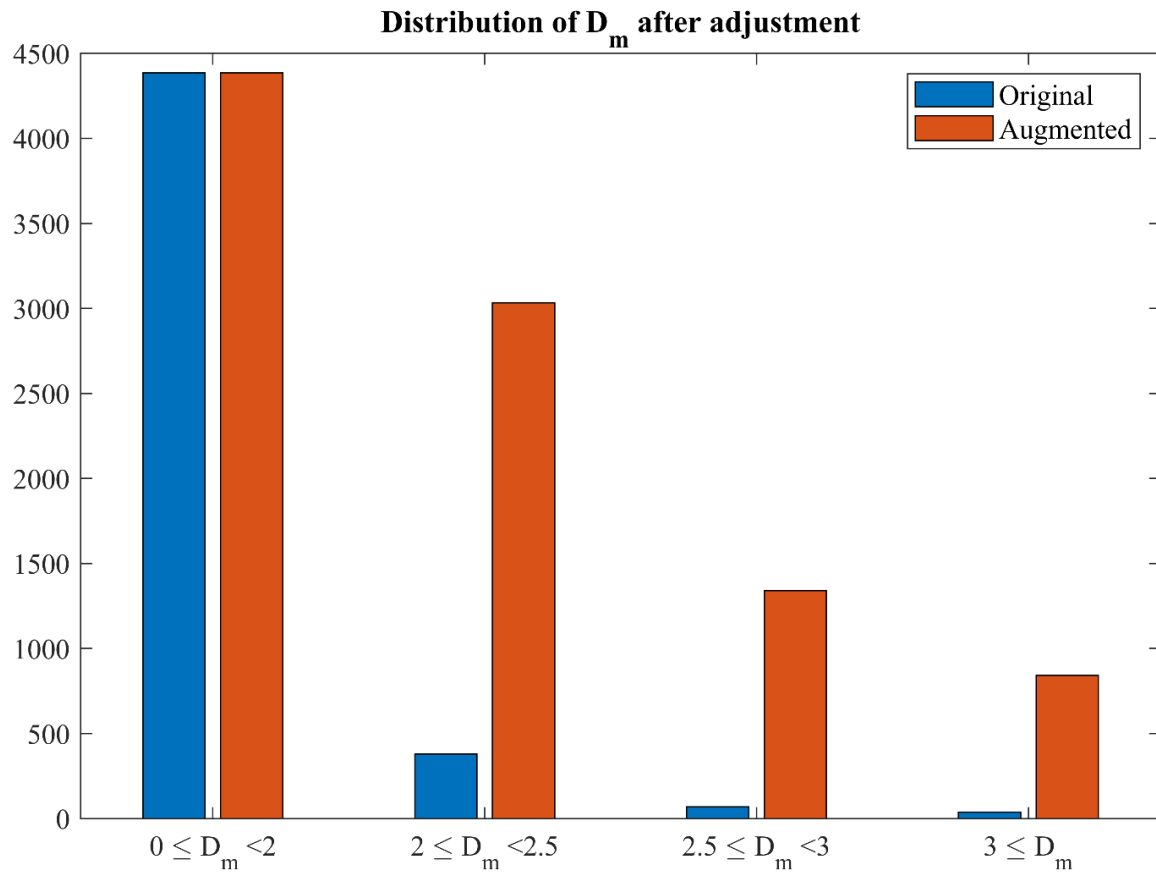
Fig. 26. Same as figure 25 except for D_m. The unit is in mm.
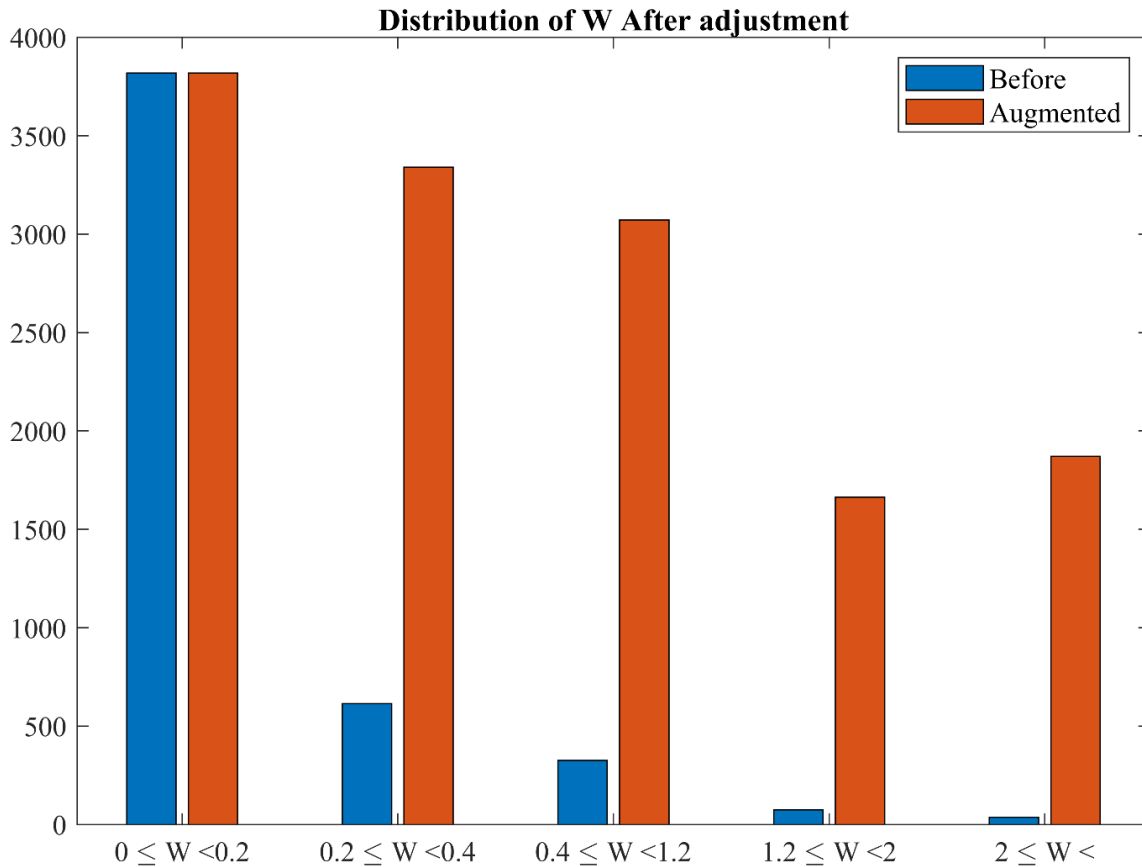
Fig. 27. Same as figure 25 except for W.

6.3 Model training with radar data

The temporal domains are separated into instantaneous (Table 15a) and rain-event-average (Table 15b). In instantaneous domain, for bias and RMSE, the DNN method shows much better skills than the empirical method (Table 15a). The DNN method indicates practically perfect performance for W and R in bias and total bias factor: bias is 0.2% for W and -2.7% for R, and total bias factor is 1 for the two variables. The bias and total bias factor might be small as positive and negative differences may have compensated each other; however, RMSE is not necessarily.

RMSE of D_m is 18.4% in DNN method, which is slightly better than 21.9% in empirical method. For W and R, RMSE values are about 100% in DNN method and 130-170% in empirical method.

Table 15. The bias, root-mean-square-error (RMSE), and total bias factor of the error estimation for the three variables (D_m, W, and R) from the radar trained and tested using the empirical (E) and DNN (D) methods. The values are shown in two temporal domains, (a) instantaneous and (b) rain-event-average. Units of bias and RMSE are %.

(a) Instantaneous domain

	D_m		W		R	
	E	D	E	D	E	D
Bias (%)	12.3	7.6	56.6	0.2	75.9	−2.7
RMSE (%)	21.9	18.4	136.5	104.8	168.9	104.4
Total bias factor	1.1	1.1	1.6	1.0	1.8	1.0

(b) Rain-event-average domain

	D_m		W		R	
	E	D	E	D	E	D
Bias (%)	14.0	7.5	44.8	−1.3	62.0	−7.0
RMSE (%)	18.1	10.3	75.8	38.5	98.7	43.0
Total bias factor	1.1	1.1	1.5	1.0	1.6	0.9

In rain-event-average domain, most extreme outliers disappear as the continuous rain rates are combined into the same rain event. The RMSE values decrease significantly in this domain; these reduce by half in both three variables and two methods (Table 15b). By contrast, the bias and total bias factor are similar or rather increased. Somehow, the total bias factor from the DNN method is 1 or close, so it indicates very good performance. Comparing to the previous research, DNN reduced rain estimation error from about 15% to less than 5%. Some of the outlying points in the 2DVD trained empirical (Figs. 22-24) results were removed using radar observation trained DNN (Figs. 28-30). However, including the large errors near x and y-axis, additional analysis of outlying points seems to be necessary.
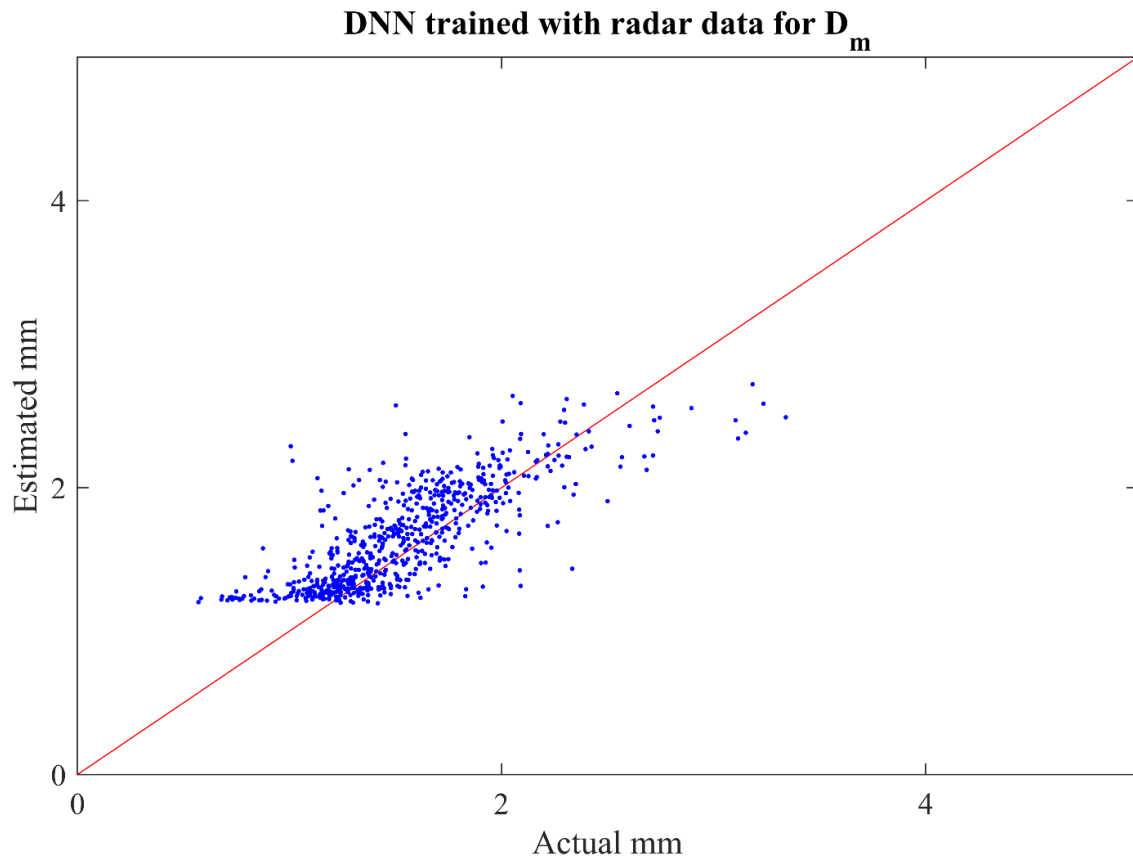
Fig. 28. D_m estimation result from radar trained DNN model.
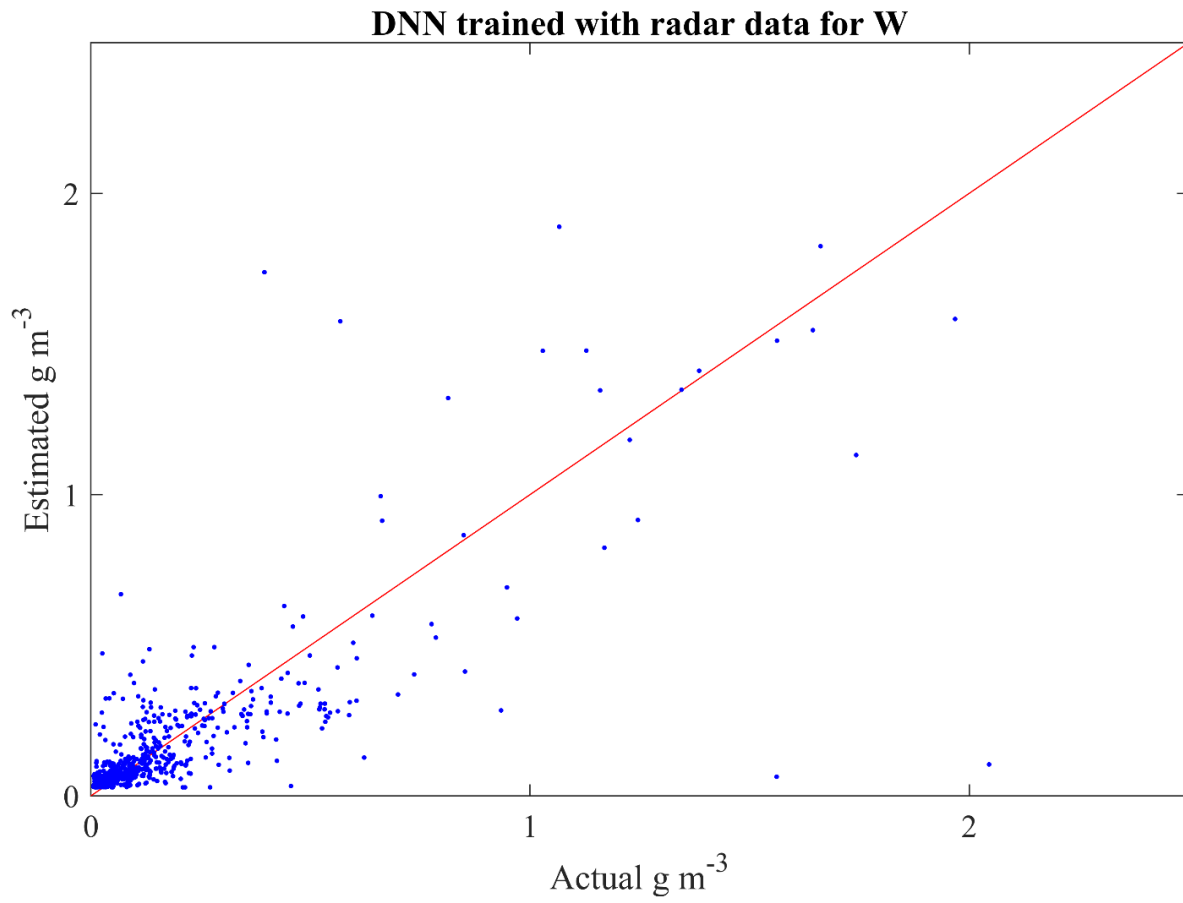
Fig. 29. Same as figure 28 except for W estimation.
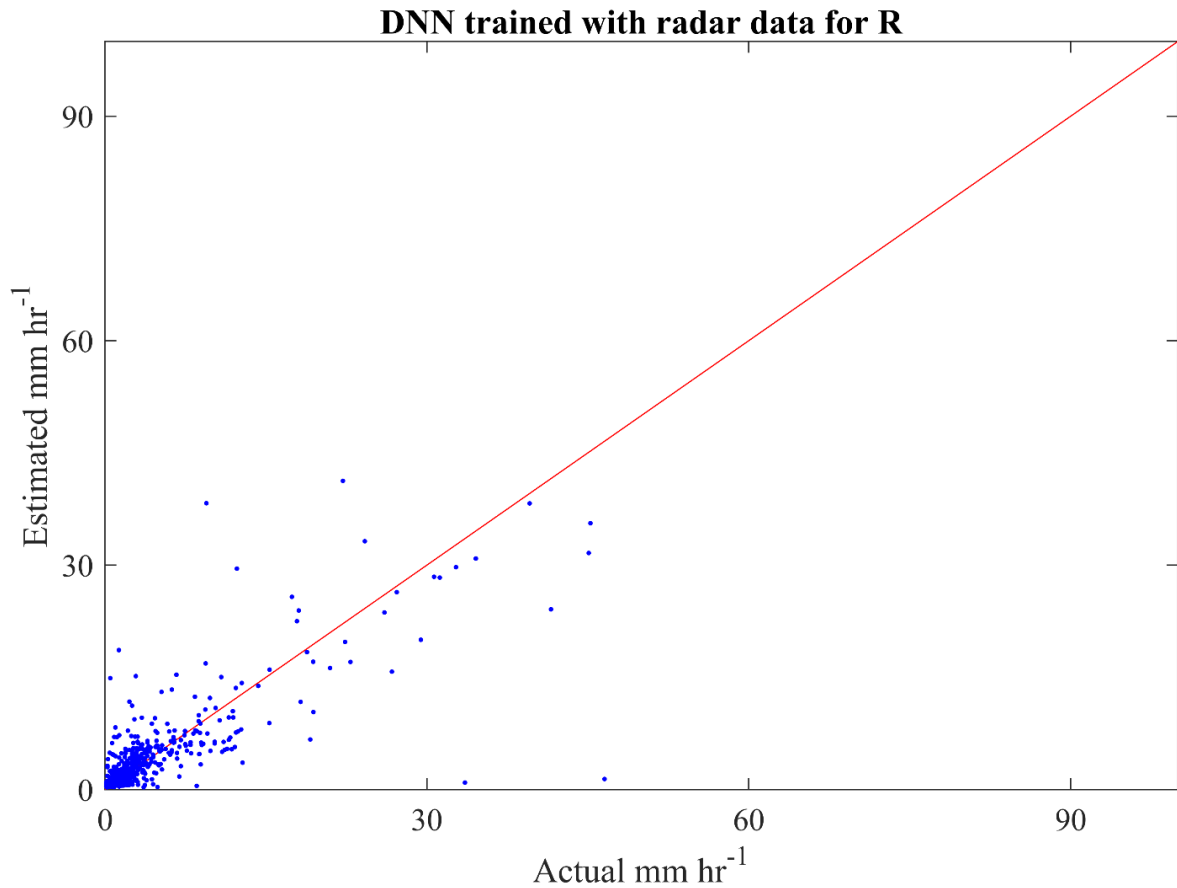
Fig. 30. Same as figure 28 except for R estimation.

From the high RMSE values, some evident outliers were noticed. From the estimation results, outliers with the largest deviations from ground observations were sorted. In total of 668 points in testing data, about 48 points showed large errors, consisting more than half of the total error. The outliers that consist of about 10% of the testing data were causing more than 50% of the errors for all training methods. It is noted that sources of contamination include but not limited to ground clutter and anomalous propagation, hail contamination, inhomogeneous rain, heavy rain, and infrequent large drops. The outliers resulted from the prementioned physical reasons do not show significant improvements regardless of the methods used. While efforts to remove the influence

from ground clutter, hail or other hydrometeors were conducted, the influence from nearby gates or rays were difficult to mitigate. Overall, similar results were found for both empirical and DNN (Table 16) in terms of outlying points, as implied in such high RMSE. In order for huge improvements in DSD retrieval and rain estimation, thorough analysis of the outliers seems to be needed.

Table 16. The bias, root-mean-square-error (RMSE), and total bias factor of the error estimation for the three variables (D_m, W, and R) from the 2DVD trained the empirical (E) and radar trained DNN (D) methods tested on radar data excluding influence of other hydrometeors. The values are shown in two temporal domains, (a) instantaneous and (b) rain-event-average. Units of bias and RMSE are %.

(a) Instantaneous domain

	D_m		W		R	
	E	D	E	D	E	D
Bias (%)	5.1	5.6	−3.1	−2.0	2.4	2.9
RMSE (%)	16.4	18.6	122.4	95.4	144.7	101.6
Total bias factor	1.1	1.1	1.0	1.0	1.0	1.0

(b) Rain-event-average domain

	D_m		W		R	
	E	D	E	D	E	D
Bias (%)	5.4	6.7	−13.7	−13.3	−8.8	−10.2
RMSE (%)	7.4	8.8	89.1	78.5	93.9	78.3
Total bias factor	1.1	1.1	0.9	0.9	0.9	0.9

There are 23 rain-event-average cases for the testing period of January - July 2017. Figure 29 displays testing results of D_m, W, and R using the empirical and DNN methods in the rain-event-average domain. Overall, the deviations from observations are relatively small in D_m (Fig. 31a) and large in W and R (Figs. 31b and c, respectively). When comparing the two methods, except for a few cases (e.g., 18th, 22nd, and 23rd cases), DNN method shows better performance than

empirical method. It is noted that a large amount of positive deviation appears in all three variables by empirical method in the 15th case. The DNN method yields a value close to the observation.
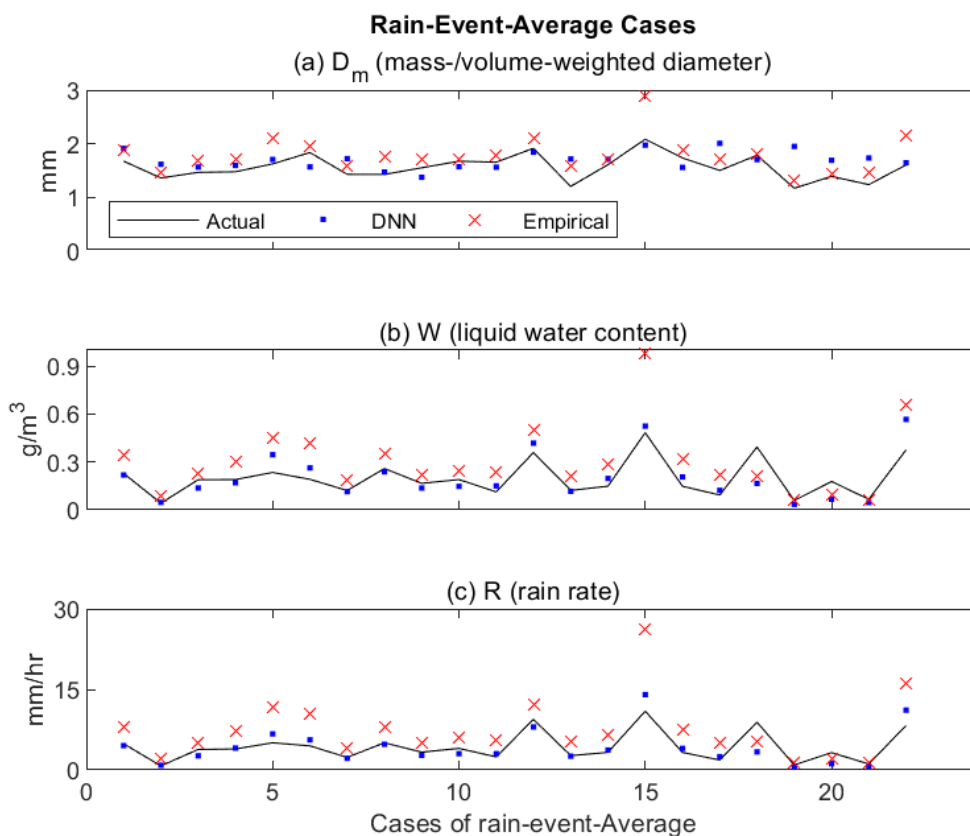
Fig. 31. The event averaged result for D_m, W, and R estimation using the radar data trained DNN and empirial formula.

7. Summary and Conclusion

The present study evaluated the radar retrievals of rain microphysics parameters (D_m, W, and R) from newly developed DNN model by comparing those from two conventional methods such as physics-based inversion and empirical formula. During the period 2006–2017, the ground-truth 2DVD located at KFFL and radar data obtained from Oklahoma City KTLX radar were analyzed.

The 2DVD data was temporally degraded into five-minute intervals to match the temporal resolution between the two datasets. Empirical and DNN methods were trained and tested on different data; partitioning of training, validation, and testing periods was 70%, 15%, and 15% in the 2DVD data and 80%, 10%, and 10% in the radar data, respectively.

First of all, the training and testing data were taken from the identical 2DVD data. The estimation results of D_m, W, and R were calculated for three error types (perfect, adding measurement, and with model) in instantaneous temporal domain. The performance of the three methods were similar for perfect and adding measurement error categories with relatively low bias. However, the estimations deteriorated when model errors were involved. In particular, the bias of physics-based inversion method was large for all D_m, W, and R estimation because this method cannot resolve non-statistical random errors. Then, the rain events that occurred continuously for longer than twenty minutes were sorted into rain-event-average. While overall results from 23 rain-event-average cases were similar to those from the instantaneous, RMSE reduced significantly in the measurement error category; the averaging process compensated for most of the gaussian errors contained in the input data.

Second, the training and testing data were obtained from two different datasets: 2DVD-trained empirical and DNN methods were applied to the radar observations for testing. Since two different datasets were used for training and testing, bias correction between the two datasets was necessary. It was found that radar observations/retrievals have negative biases compared to 2DVD data due to additional sources of errors and contamination. Two types of bias correction (i.e., with and without) and two categories of adding measurement error (i.e., with and without) in the training model were examined. When bias in the two datasets were minimized, errors of R estimation decreased 30%. In addition to bias correction, measurement errors were included in an effort to

minimize the impact of extra errors and contamination in radar data. With this gaussian error in the training model, less sensitivity to radar-induced errors were found. This extra error inclusion reduced about 10% bias for D_m estimation using DNN. Similar results were shown for rain-event-average analysis.

Third, both training and testing were conducted on radar observation data for empirical and DNN methods. Disdrometer variables are observed periodically with much smaller spatiotemporal volume compared to radar. In addition, the bias between the 2DVD and radar varies significantly based on the distance between the two observation locations (Tokay et al. 2020). Thus, direct training from radar data may be helpful. About 50,000 minutes and 3,000 minutes of radar data were used for training and testing, respectively. For instantaneous retrieval and estimation, the bias for DNN method was 7.6, -0.2, and -2.7% for D_m, W, and R, respectively. The bias for empirical method was higher with 12.3, 56.6, 75.9, for D_m, W, and R, respectively. Similar results were also shown for rain-event-average computations. Summing up, DNN method may provide about 70% and 50% improvements for R estimation and DSD retrieval, respectively, when radar data are utilized for both training and testing.

Since the DNN algorithm includes nonlinear terms, which were not included in the empirical method, comprehensive representations between the estimators and radar variables are anticipated. This study represents the superiority of DNN in radar-retrievals of rain rate and physical parameters. However, there are several weaknesses and potential for future improvements in the present analysis. While impact of statistical and random errors was reduced using DNN, much of the outliers occurring from physical reasons, such as ground clutter, hail contamination, inhomogeneous rain, and heavy rain, requires additional improvements. Even after the removal of anomalous propagation, hail clutter, and influence of other hydrometeors, large errors existed.

While the source and reason of errors in DSD retrieval and QPE are relatively well known, there had been lack of tools to incorporate multiple polarimetric and/or meteorological signatures to solve those issues. The complexity of statistical methods increases rapidly when number of input and output variables and parameters increase. DNN is one of the simplest forms of deep learning available at present, with more complex models such as long short-term memory network and convolutional neural network are available. It is noted that simple forms often showed better performance compared to complicated ones (Schultz et al. 2021), thus verification of usage of neural networks for DSD retrieval and QPE were required. In this study, neural networks showed the potential to provide accurate and less biased retrieval and estimations. Next, polarimetric and meteorological signatures that may be included in the deep learning model should be located. Deep learning is most useful to solve complex problems that are often hard to from using empirical or statistical methods. Thus, integrating the polarimetric signatures and other meteorological variables from vertical profiles and/or spatiotemporal information of the entire storm motion may enhance the retrievals. In addition, DSD retrieval and QPE should be further improved to include different types of hydrometeors, and/or various mixture of hydrometeors. DNN also has critical weakness in its inability to exactly describe why and how the errors are decreased compared to the physics-based inversion retrieval or empirical formulas. Newly developed AI algorithms may be used to deliver some interpretability in its hidden layers. The inclusion of observational errors, and incorporations of additional phases of hydrometeors using further advanced machine learning techniques may improve rain estimation using ground-based radars in remote areas, our understanding of cloud microphysics and radiative properties, and weather forecasts. More efforts to understand the results scientifically are required.

References

Alimissis, A., Philippopoulos, K., Tzanis, C. G., & Deligiorgi, D. (2018). Spatial estimation of urban air pollution with the use of artificial neural network models. *Atmospheric Environment*, *191*, 205–213. doi:10.1016/j.atmosenv.2018.07.058

Alzubaidi, L., Zhang, J., Humaidi, A. J., Al-Dujaili, A., Duan, Y., Al-Shamma, O., et al. (2021). Review of Deep Learning: Concepts, CNN Architectures, challenges, applications, Future Directions. *Journal of Big Data*, *8*(1). doi:10.1186/s40537-021-00444-8

Brandes, E. A., Ryzhkov, A. V., & Zrnić Dušan S. (2001). An evaluation of radar rainfall estimates from specific differential phase. *Journal of Atmospheric and Oceanic Technology*, *18*(3), 363–375. doi:10.1175/1520-0426(2001)018<0363:aeorre>2.0.co;2

Brandes, E. A., G. Zhang, and J. Vivekanandan, 2002: Experiments in rainfall estimation with a polarimetric radar in a subtropical environment. *Journal of Applied Meteorology*, **41**, 674–685, doi:10.1175/1520-0450(2002)041<0674:eirewa>2.0.co;2.

Bukovčić, P., D. Zrnić, and G. Zhang, 2015: Convective–stratiform separation using video disdrometer observations in Central Oklahoma – the Bayesian approach. *Atmospheric Research*, **155**, 176–191, doi:10.1016/j.atmosres.2014.12.002.

Campesato, O. (2020). *Artificial Intelligence, Machine Learning, and Deep Learning*. Dulles, VA: Mercury Learning and Information.

Campos, E. and I. Zawadzki. 2000. Instrument uncertainties in *Z–R* relations. *J. Appl. Meteor* 39:1088–1102.

Cao, Q., G. Zhang, E. A. Brandes, and T. J. Schuur, 2010: Polarimetric radar rain estimation through retrieval of drop size distribution using a Bayesian approach. *Journal of Applied Meteorology and Climatology*, **49**, 973–990, doi:10.1175/2009jamc2227.1.

Cao, Q., G. Zhang, E. Brandes, T. Schuur, A. Ryzhkov, and K. Ikeda, 2008: Analysis of video disdrometer and polarimetric radar data to characterize rain microphysics in Oklahoma. *Journal of Applied Meteorology and Climatology*, **47**, 2238–2255, doi:10.1175/2008jamc1732.1.

Chen, H., V. Chandrasekar, and R. Cifelli, 2019: A deep learning approach to dual-polarization radar rainfall estimation. *2019 URSI Asia-Pacific Radio Science Conference (AP-RASC)*, doi:10.23919/ursiap-rasc.2019.8738337.

Chen, H., Chandrasekar, V., Cifelli, R., & Xie, P. (2020). A machine learning system for precipitation estimation using satellite and Ground Radar Network Observations. *IEEE Transactions on Geoscience and Remote Sensing*, *58*(2), 982–994. doi:10.1109/tgrs.2019.2942280

Cui, X., Goel, V., & Kingsbury, B. (2014). Data Augmentation for Deep Neural Network Acoustic modeling. *2014 IEEE International Conference on Acoustics, Speech and Signal Processing (ICASSP)*. doi:10.1109/icassp.2014.6854671

Danielsen, E. F., Bleck, R., & Morris, D. A. (1972). Hail growth by stochastic collection in a cumulus model. *Journal of the Atmospheric Sciences*, *29*(1), 135–155. doi:10.1175/1520-0469(1972)029<0135:hgbsci>2.0.co;2

Doviak, R. J., and Zrníc Dúsn S., 1984, 1993: *Doppler radar and weather observations*. Academic Press, San Diego, CA.

Grams, H. M. (2019). Dual polarization quantitative precipitation estimation on the WSR-88D: Current status and future plans. *AMS supported meetings*. AMS. https://ams.confex.com/ams/2019Annual/webprogram/Paper352300.html. Accessed 26 July 2022

Haddad, Z. S., Durden, S. L., & Im, E. (1996). Parameterizing the raindrop size distribution. *Journal of Applied Meteorology*, *35*(1), 3–13. doi:10.1175/1520-0450(1996)035<0003:ptrsd>2.0.co;2

Ho, C.-H., Park, I., Oh, H.-R., Gim, H.-J., Hur, S.-K., Kim, J., & Choi, D.-R. (2021). Development of a PM2.5 prediction model using a recurrent neural network algorithm for the Seoul Metropolitan Area, Republic of Korea. *Atmospheric Environment*, *245*, 118021. doi:10.1016/j.atmosenv.2020.118021

Huaman, L., & Schumacher, C. (2018). Assessing the vertical latent heating structure of the East Pacific Itcz using the *cloudsat* CPR and TRMM PR. *Journal of Climate*, *31*(7), 2563–2577. doi:10.1175/jcli-d-17-0590.1

Hubbert, J. C., Dixon, M., Ellis, S. M., & Meymaris, G. (2009). Weather radar ground clutter. part I: Identification, modeling, and simulation. *Journal of Atmospheric and Oceanic Technology*, *26*(7), 1165–1180. doi:10.1175/2009jtecha1159.1

Janiesch, C., Zschech, P., & Heinrich, K. (2021, October 13). Machine learning and deep learning - electronic markets. *SpringerLink*. Springer Berlin Heidelberg. https://link.springer.com/article/10.1007/s12525-021-00475-2. Accessed 26 July 2022

Kessler, E. (1969). On the distribution and continuity of water substance in atmospheric circulations. *On the Distribution and Continuity of Water Substance in Atmospheric Circulations*, 1–84. doi:10.1007/978-1-935704-36-2_1

Kim, H. I., & Han, K. Y. (2020). Urban flood prediction using deep neural network with data augmentation. *Water*, *12*(3), 899. doi:10.3390/w12030899

Kingma, Diederik P. and Ba, Jimmy. Adam: A method for stochastic optimization. CoRR, abs/1412.6980, 2014.

Kruger, A., and W. F. Krajewski, 2002: Two-dimensional video disdrometer: A description. *Journal of Atmospheric and Oceanic Technology*, **19**, 602–617, doi:10.1175/1520-0426(2002)019<0602:tdvdad>2.0.co;2.

Kozu, T., & Nakamura, K. (1991). Rainfall parameter estimation from dual-radar measurements combining reflectivity profile and path-integrated attenuation. *Journal of Atmospheric and Oceanic Technology*, *8*(2), 259–270. doi:10.1175/1520-0426(1991)008<0259:rpefdr>2.0.co;2

Kumjian, M. (2013). Principles and applications of dual-polarization weather radar. part I: Description of the polarimetric radar variables. *Journal of Operational Meteorology*, *1*(19), 226–242. doi:10.15191/nwajom.2013.0119

Kusiak, A., X. Wei, A. P. Verma, and E. Roz, 2013: Modeling and prediction of rainfall using radar reflectivity data: A data-mining approach. *IEEE Transactions on Geoscience and Remote Sensing*, **51**, 2337–2342, doi:10.1109/tgrs.2012.2210429.

Lang, R. M., Addetia, K., Miyoshi, T., Kebed, K., Blitz, A., Schreckenberg, M., et al. (2021). Use of machine learning to improve echocardiographic image interpretation workflow: A disruptive paradigm change? *Journal of the American Society of Echocardiography*, *34*(4), 443–445. doi:10.1016/j.echo.2020.11.017

Lim, K.-S. S., & Hong, S.-Y. (2010). Development of an effective double-moment cloud microphysics scheme with prognostic cloud condensation nuclei (CCN) for weather and climate models. *Monthly Weather Review*, *138*(5), 1587–1612. doi:10.1175/2009mwr2968.1

Liu, H., & Chandrasekar, V. (2000). Classification of hydrometeors based on polarimetric radar measurements: Development of Fuzzy Logic and neuro-fuzzy systems, and in situ verification. *Journal of Atmospheric and Oceanic Technology*, *17*(2), 140–164. doi:10.1175/1520-0426(2000)017<0140:cohbop>2.0.co;2

Mahale, V. N., G. Zhang, M. Xue, J. Gao, and H. D. Reeves, 2019: Variational retrieval of rain microphysics and related parameters from polarimetric radar data with a parameterized operator. *Journal of Atmospheric and Oceanic Technology*, **36**, 2483–2500, doi:10.1175/jtech-d-18-0212.1.

Makridakis, S., Spiliotis, E., & Assimakopoulos, V. (2018). Statistical and machine learning forecasting methods: Concerns and Ways Forward. *PLOS ONE*, *13*(3). doi:10.1371/journal.pone.0194889

Marshall, J. S., & Palmer, W. M. (1948). The distribution of raindrops with size. *Journal of Meteorology*, *5*(4), 165–166. doi:10.1175/1520-0469(1948)005<0165:tdorws>2.0.co;2

Marzano, F. S., Vulpiani, G., & Rose, W. I. (2006). Microphysical characterization of microwave radar reflectivity due to Volcanic Ash Clouds. *IEEE Transactions on Geoscience and Remote Sensing*, *44*(2), 313–327. doi:10.1109/tgrs.2005.861010

Matrosov, S. Y., Kingsmill, D. E., Martner, B. E., & Ralph, F. M. (2005). The utility of X-band polarimetric radar for quantitative estimates of rainfall parameters. *Journal of Hydrometeorology*, *6*(3), 248–262. doi:10.1175/jhm424.1

May, P. T., Keenan, T. D., Zrnić, D. S., Carey, L. D., & Rutledge, S. A. (1999). Polarimetric radar measurements of tropical rain at a 5-cm wavelength. *Journal of Applied Meteorology*, *38*(6), 750–765. doi:10.1175/1520-0450(1999)038<0750:prmotr>2.0.co;2

Mikolajczyk, A., & Grochowski, M. (2018). Data augmentation for improving deep learning in image classification problem. *2018 International Interdisciplinary PhD Workshop (IIPhDW)*. doi:10.1109/iiphdw.2018.8388338

Morrison, H., & Milbrandt, J. A. (2015). Parameterization of cloud microphysics based on the prediction of bulk ice particle properties. part I: Scheme description and idealized tests. *Journal of the Atmospheric Sciences*, *72*(1), 287–311. doi:10.1175/jas-d-14-0065.1

Nelson, E. L., & L'Ecuyer, T. S. (2018). Global character of latent heat release in oceanic warm rain systems. *Journal of Geophysical Research: Atmospheres*, *123*(10), 4797–4817. doi:10.1002/2017jd027844

Nelson, E. L., L'Ecuyer, T. S., Saleeby, S. M., Berg, W., Herbener, S. R., & van den Heever, S. C. (2016). Toward an algorithm for estimating latent heat release in Warm Rain Systems. *Journal of Atmospheric and Oceanic Technology*, *33*(6), 1309–1329. doi:10.1175/jtech-d-15-0205.1

Nwankpa, C., Ijomah, W., Gachagan, A., & Marshall, S. (2018, November 8). Activation functions: Comparison of trends in practice and research for Deep Learning. *arXiv.org*. https://arxiv.org/abs/1811.03378. Accessed 26 July 2022

Park, H. S., Ryzhkov, A. V., Zrnić, D. S., & Kim, K.-E. (2009). The hydrometeor classification algorithm for the polarimetric WSR-88D: Description and application to an MCS. *Weather and Forecasting*, *24*(3), 730–748. doi:10.1175/2008waf2222205.1

Rajula, H. S., Verlato, G., Manchia, M., Antonucci, N., & Fanos, V. (2020). Comparison of conventional statistical methods with machine learning in medicine: Diagnosis, drug development, and treatment. *Medicina*, *56*(9), 455. doi:10.3390/medicina56090455

Reichstein, M., Camps-Valls, G., Stevens, B., Jung, M., Denzler, J., Carvalhais, N., & Prabhat. (2019). Deep learning and process understanding for data-driven Earth System Science. *Nature*, *566*(7743), 195–204. doi:10.1038/s41586-019-0912-1

Rosenfeld, D., and C. W. Ulbrich, 2003: Cloud microphysical properties, processes, and rainfall estimation opportunities. *Meteorological Monographs*, **30**, 237–237, doi:10.1175/0065-9401(2003)030<0237:cmppar>2.0.co;2.

Ryu, J., Song, H. J., Sohn, B. J., & Liu, C. (2021). Global distribution of three types of drop size distribution representing heavy rainfall from GPM/DPR Measurements. *Geophysical Research Letters*, *48*(3). doi:10.1029/2020gl090871

Ryzhkov, A., & Zrnić, D. (1996). Assessment of rainfall measurement that uses specific differential phase. *Journal of Applied Meteorology*, *35*(11), 2080–2090. doi:10.1175/1520-0450(1996)035<2080:aormtu>2.0.co;2

Ryzhkov, A. V., Giangrande, S. E., Melnikov, V. M., & Schuur, T. J. 2005a. Calibration issues of dual-polarization radar measurements. *Journal of Atmospheric and Oceanic Technology*, *22*(8), 1138–1155. doi:10.1175/jtech1772.1

Ryzhkov, A. V., S. E. Giangrande, and T. J. Schuur, 2005b: Rainfall estimation with a polarimetric prototype of WSR-88D. *Journal of Applied Meteorology*, **44**, 502–515, doi:10.1175/jam2213.1.

Ryzhkov, A., Pinsky, M., Pokrovsky, A., & Khain, A. (2011). Polarimetric radar observation operator for a cloud model with spectral microphysics. *Journal of Applied Meteorology and Climatology*, *50*(4), 873–894. doi:10.1175/2010jamc2363.1

Ryzhkov, A., Zhang, P., Bukovčić, P., Zhang, J., & Cocks, S. (2022). Polarimetric radar quantitative precipitation estimation. *Remote Sensing*, *14*(7), 1695. doi:10.3390/rs14071695

Sachidananda, M., & Zrnić, D. S. (1987). Rain rate estimates from differential polarization measurements. *Journal of Atmospheric and Oceanic Technology*, *4*(4), 588–598. doi:10.1175/1520-0426(1987)004<0588:rrefdp>2.0.co;2

Sarker, I. H., 2021: Machine learning: Algorithms, real-world applications and Research Directions. *SN Computer Science*, **2**, doi:10.1007/s42979-021-00592-x.

Schultz, M. G., Betancourt, C., Gong, B., Kleinert, F., Langguth, M., Leufen, L. H., et al. (2021). Can deep learning beat numerical weather prediction? *Philosophical Transactions of the Royal Society A: Mathematical, Physical and Engineering Sciences*, *379*(2194), 20200097. doi:10.1098/rsta.2020.0097

Seliga, T. A., and V. N. Bringi, 1976: Potential use of radar differential reflectivity measurements at orthogonal polarizations for measuring precipitation. *Journal of Applied Meteorology*, **15**, 69–76, doi:10.1175/1520-0450(1976)015<0069:puordr>2.0.co;2.

Seliga, T. A., Bringi, V. N., & Al-khatib, H. H. (1979). Differential reflectivity measurements in rain: First experiments. *IEEE Transactions on Geoscience Electronics*, *17*(4), 240–244. doi:10.1109/tge.1979.294652

Shin, K., J. J. Song, W. Bang, and G. W. Lee, 2021: Quantitative precipitation estimates using machine learning approaches with operational dual-polarization Radar Data. *Remote Sensing*, **13**, 694, doi:10.3390/rs13040694.

Smith, P. L., Myers, C. G., & Orville, H. D. (1975). Radar reflectivity factor calculations in numerical cloud models using bulk parameterization of precipitation. *Journal of Applied Meteorology*, *14*(6), 1156–1165. doi:10.1175/1520-0450(1975)014<1156:rrfcin>2.0.co;2

Szandała, T. (2020). Review and comparison of commonly used activation functions for deep neural networks. *Bio-inspired Neurocomputing*, 203–224. doi:10.1007/978-981-15-5495-7_11

Testud, J., Le Bouar, E., Obligis, E., & Ali-Mehenni, M. (2000). The rain profiling algorithm applied to polarimetric weather radar. *Journal of Atmospheric and Oceanic Technology*, *17*(3), 332–356. doi:10.1175/1520-0426(2000)017<0332:trpaat>2.0.co;2

Thurai, M., Bringi, V., Wolff, D., Marks, D. A., Gatlin, P. N., & Wingo, M. T. (2021). Retrieving rain drop size distribution moments from GPM dual-frequency precipitation radar. *Remote Sensing*, *13*(22), 4690. doi:10.3390/rs13224690

Tokay, A., L. P. D'Adderio, D. A. Marks, J. L. Pippitt, D. B. Wolff, and W. A. Petersen, 2020: Comparison of raindrop size distribution between NASA's S-band Polarimetric radar and two-dimensional video disdrometers. *Journal of Applied Meteorology and Climatology*, **59**, 517–533, doi:10.1175/jamc-d-18-0339.1.

Tokay, A., P. G. Bashor, E. Habib, and T. Kasparis, 2008: Raindrop size distribution measurements in tropical cyclones. *Monthly Weather Review*, **136**, 1669–1685, doi:10.1175/2007mwr2122.1.

Tokay, A., & Short, D. A. (1996). Evidence from tropical raindrop spectra of the origin of rain from stratiform versus convective clouds. *Journal of Applied Meteorology*, *35*(3), 355–371. doi:10.1175/1520-0450(1996)035<0355:eftrso>2.0.co;2

Ulbrich, C. W. (1983). Natural variations in the analytical form of the Raindrop Size Distribution. *Journal of Climate and Applied Meteorology*, *22*(10), 1764–1775. doi:10.1175/1520-0450(1983)022<1764:nvitaf>2.0.co;2

Ulbrich, C. W., & Atlas, D. (1984). Assessment of the contribution of differential polarization to improved rainfall measurements. *Radio Science*, *19*(1), 49–57. doi:10.1029/rs019i001p00049

Ulbrich, C. W., & Lee, L. G. (1999). Rainfall measurement error by WSR-88D radars due to variations in *Z–r* law parameters and the radar constant. *Journal of Atmospheric and Oceanic Technology*, *16*(8), 1017–1024. doi:10.1175/1520-0426(1999)016<1017:rmebwr>2.0.co;2

Vivekanandan, J., Adams, W. M., & Bringi, V. N. (1991). Rigorous approach to polarimetric radar modeling of Hydrometeor orientation distributions. *Journal of Applied Meteorology*, *30*(8), 1053–1063. doi:10.1175/1520-0450(1991)030<1053:ratprm>2.0.co;2

Y. Xu, R. Jia, L. Mou, G. Li, Y. Chen, Y. Lu, and Z. Jin. Improved relation classification by deep recurrent neural networks with data augmentation. CoRR, abs/1601.03651, 2016.

Zhang, G., Vivekanandan, J., & Brandes, E. (2001). A method for estimating rain rate and drop size distribution from polarimetric radar measurements. *IEEE Transactions on Geoscience and Remote Sensing*, *39*(4), 830–841. doi:10.1109/36.917906

Zhang, G., 2016: Weather Radar Polarimetry. CRC Press, 304 pp.

Zhang, G., and Coauthors, 2019: Current status and future challenges of weather radar polarimetry: Bridging the gap between Radar Meteorology/hydrology/engineering and numerical weather prediction. *Advances in Atmospheric Sciences*, **36**, 571–588, doi:10.1007/s00376-019-8172-4.

Zhang, G., Gao, J., & Du, M. (2021). Parameterized forward operators for simulation and assimilation of polarimetric radar data with numerical weather predictions. *Advances in Atmospheric Sciences*, *38*(5), 737–754. doi:10.1007/s00376-021-0289-6

Zhang, J., Tang, L., Cocks, S., Zhang, P., Ryzhkov, A., Howard, K., et al. (2020). A dual-polarization radar synthetic QPE for Operations. *Journal of Hydrometeorology*, *21*(11), 2507–2521. doi:10.1175/jhm-d-19-0194.1

Zhao, Y., Wang, G., Tang, C., Luo, C., Zeng, W., & Zha, Z.-J. (2021, November 25). A Battle of Network Structures: An empirical study of CNN, Transformer, and MLP. *arXiv.org*. https://arxiv.org/abs/2108.13002. Accessed 26 July 2022